

## Research paper

## A viscoplastic recoverable sensitivity model for fine-grained soils

Vikram Singh<sup>a,\*</sup>, Sam Stanier<sup>b</sup>, Britta Bienen<sup>a</sup>, Mark F. Randolph<sup>a</sup><sup>a</sup> Centre for Offshore Foundation Systems, University of Western Australia, Perth, WA 6009, Australia<sup>b</sup> Cambridge University Engineering Department, Trumpington Street, Cambridge, CB2 1PZ, UK

## ARTICLE INFO

## Keywords:

Constitutive modelling

Rate-dependency

Strain-softening-hardening

Sensitivity recovery

Large deformation finite element analyses

T-bar penetration tests

## ABSTRACT

Full-flow penetrometer testing in fine-grained soils indicates that undrained shear strength decreases due to remoulding induced generation of excess pore pressures and increases due to strain rate effects and dissipation of excess pore pressures. This paper presents a viscoplastic strain-softening-hardening constitutive model that captures this duality of behaviour via non-local regularisation, strain rate dependency, and consolidation induced recovery of sensitivity. The model is based on Structured Modified Cam Clay and Perzyna's overstress framework. Validation of the implementation is first demonstrated through simulation of constant rate of strain triaxial and oedometer compression tests performed on different clays. The model is then applied in large deformation finite element analyses of monotonic and variable rate T-bar penetration to demonstrate successful numerical implementation and its ability to simulate strain rate effects. Finally, the model is applied in the simulation of undrained cycles of penetration of a T-bar penetrometer in kaolin clay and a carbonate silt and compared with data from geotechnical centrifuge experiments. The results show that the model without sensitivity recovery significantly underestimates the consolidated-undrained resistance in both soils, suggesting that recoverable sensitivity is an aspect of behaviour that ought to be considered in the development of constitutive models for soft sensitive soils.

## 1. Introduction

The design and stability analyses of offshore structures, particularly those founded on soft fine-grained sediments, are significantly influenced by changing soil strength due to episodes (events) of undrained remoulding and intermittent periods of re-consolidation. In geotechnical processes such as full-flow penetrometer testing, anchor installation, keying and pullout, pipe laying and buckling, soils exhibit strain-softening behaviour during rapid undrained loading, with development of excess pore pressures and a gradual loss of undrained shearing resistance. Subsequent dissipation of the excess pore pressures induces strain-hardening of the soil, resulting in recovered or even increased strength. This duality of the soil behaviour has been investigated by T-bar penetrometer test in soft kaolin clay by Hodder et al. (2013), as reproduced in Fig. 1, which presents three episodes of twenty undrained cycles with a consolidation period between each undrained episode that facilitated complete dissipation of excess pore pressures. Degradation of the shear strength and sensitivity occurs due to repeated cycling in each episode, reaching an asymptotic state in each packet of cycles. During the intervening dissipation periods, some regain of both strength and sensitivity occurs due to re-consolidation that can be observed from the measured T-bar data of the second and third undrained packets of cycles.

Consolidation induced strength regain can be theoretically quantified by the ratio of current undrained shear strength ( $s_u$ ) and its theoretical drained limit ( $s_{u-d}$ ),  $s_u/s_{u-d}$ . The theoretical drained limit,  $s_{u-d}$ , referred to here is the limiting undrained shear strength  $s_u$  that occurs when the void ratio and effective stress state become asymptotic. This typically occurs after several cycles of remoulding (generation of excess pore pressure) and excess pore pressure dissipation (consolidation) and the potential for further generation of excess pore pressure diminishes and the undrained and drained shear resistance are equivalent. Complete sensitivity regain will result in an  $s_u/s_{u-d}$  ratio of 1 as the cyclic stress state approaches the initial state at the end of the dissipation process. Values of  $s_u/s_{u-d} < 1$  indicates the loss of some sensitivity possibly due to loss of fabric or inter-particle structure initially present in the soil which cannot be recovered by dissipation of excess pore pressures alone.

The potential regain of the strength due to consolidation is illustrated in Fig. 2, with use of the data derived from the T-bar penetrometer tests in soft kaolin clay and carbonate silt by Cocjin et al. (2014) and Jia (2021), respectively, involving cycles of penetration and full extraction with a period sufficiently long to facilitate full dissipation of excess pore pressures between each cycle. Fig. 2a and c present the penetration resistance ( $q_{pen}$ ) against depth ( $z$ ) for the two soils.

\* Corresponding author.

E-mail address: [vikram.singh@research.uwa.edu.au](mailto:vikram.singh@research.uwa.edu.au) (V. Singh).

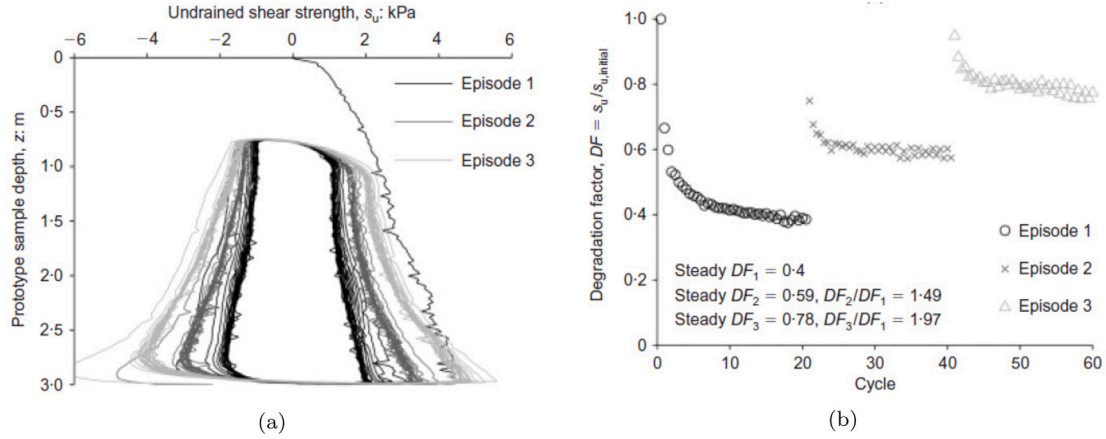


Fig. 1. Cyclic T-bar penetration test with dissipation between cyclic undrained episodes demonstrating changing shear strength due to strain softening and hardening: (a) undrained strength against sample depth, and (b) strength degradation factor against penetration cycle number (after Hodder et al., 2013).

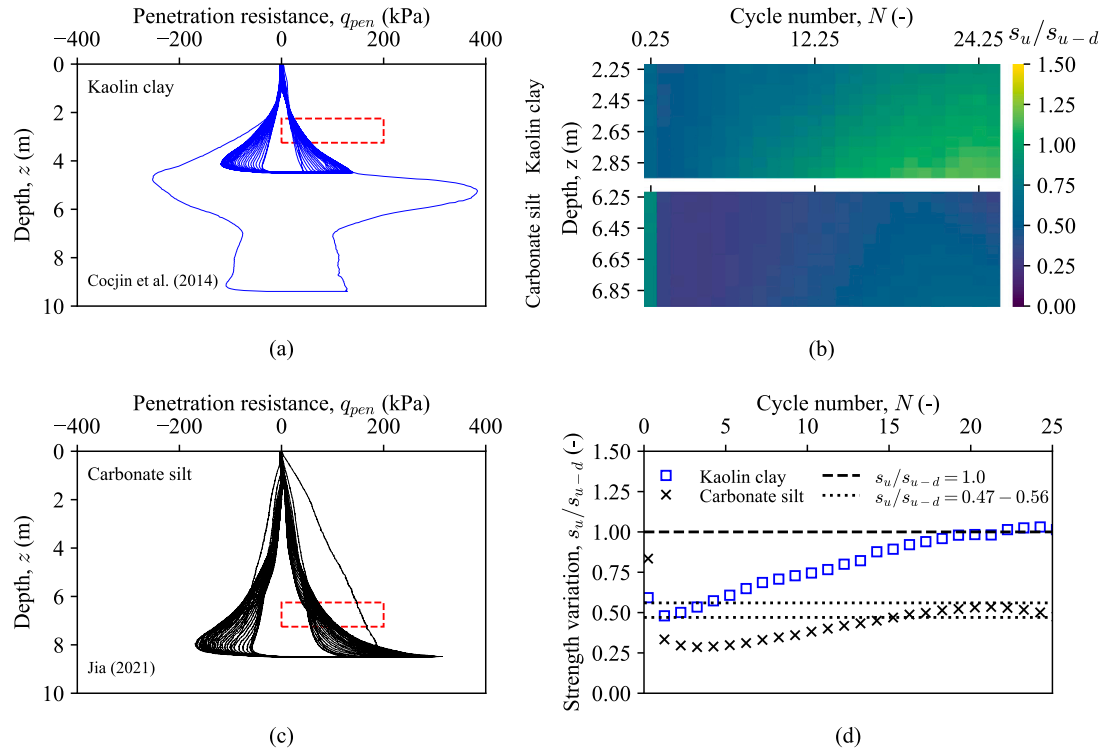


Fig. 2. Strain-softening and hardening induced by episodic undrained cycles of T-bar penetration with dissipation periods between each cycle with the T-bar positioned at the soil surface: (a,c) penetration resistance vs. depth; (b) heat maps of  $s_u / s_{u-d}$ ; and (d) average  $s_u / s_{u-d}$  vs.  $N$ .

Theoretically the regain of sensitivity can be inferred by normalising the current undrained strength ( $s_u$ ) mobilised in subsequent packets of cycles (post re-consolidation) by the theoretical drained limit ( $s_{u-d}$ ). A value equal to the inverse of the initial sensitivity indicates no recovery of sensitivity, and a value of unity indicates full recovery of sensitivity. The current undrained shear strength,  $s_u$ , at all depths  $z_i$  after  $N$  cycles is directly calculated from the measured T-bar resistance ( $q_{pen}$ ) using a breakout factor  $N_c$  of 10.5 from plasticity solutions (Randolph and Houlsby, 1984), given as:

$$s_u = \frac{q_{pen}}{10.5} \quad (1)$$

which assumes an intermediate T-bar surface roughness. The value of  $s_{u-d}$  assuming plane strain deformation in the T-bar penetration can be

estimated using the following relationship:

$$s_{u-d} = \frac{2}{\sqrt{3}} \left\{ \frac{M}{2} \frac{1 + 2(1 - \sin \phi_c)}{3} \sigma'_v \right\} \quad (2)$$

in which  $M$  is the gradient of the critical state line and  $\phi_c$  is the critical state friction angle.

Such a calculation is sensitive to the non-linear variation of effective unit weight evident in the centrifuge models analysed, so an expression for the in-situ effective unit weight ( $\gamma'$ ) for each soil was derived with respect to the depth ( $z_i$ ) based on measurements taken from each sample. A close fit was found using the following function:

$$\gamma' = a + (br^{z_i}) + (cz_i) \quad (3)$$

in which the values of fitting parameters  $a$ ,  $b$ ,  $c$ , and  $r$  were best fitted by minimising the difference between experiment and fit data. The

initial vertical effective stress  $\sigma'_{v0}$  can be calculated at a depth  $z_i$  via the following integral:

$$\sigma'_{v0} = \int_0^{z_i} \gamma' dz_i \quad (4)$$

which was solved numerically assuming a small value of  $dz_i$ . In an episodic penetration test (here episodic is used to indicate the fact that the test involves several undrained remoulding and consolidation events), the T-bar is penetrated through and extracted from the soil sample repeatedly, which sometimes creates a cavity at the free surface – often referred to as a ‘rat hole’ – at shallow depths in the soil. The depth of this ‘rat hole’ increases with the number of penetration and extraction cycles ( $N$ ) and leads to a slight reduction in overburden stresses in the underlying soil, resulting in a lightly over-consolidated stress state in the soil involved in the subsequent failure mechanism. The depth of the ‘rat hole’  $z_r$  for each cycle of penetration was determined from the penetration resistance data (Fig. 2a and c) as the depth at which the penetration resistance,  $q_{pen}$ , suddenly deviates from a near zero value to an increasing nonzero value with depth. Again assuming that no soil is present in the ‘rat hole’, the current vertical effective stresses  $\sigma'_v$  after any number of T-bar cycles can be calculated using:

$$\sigma'_v = \int_0^{z_i} \gamma' dz_i - \int_0^{z_r} \gamma' dz_r \quad (5)$$

which was once again solved numerically assuming a small value of  $dz_i$ .

This system of equations produced the heat-maps of the strength ratio,  $s_u/s_{u-d}$ , which were extracted from a one metre depth window (at prototype depths, model depth  $\times$  centrifuge  $g$  level, of 2.25–3.25 m and 6.25–7.25 m for kaolin clay and carbonate silt, respectively), are presented in Fig. 2b for a total of 25 cycles of penetration. The tests were carried out in the geotechnical centrifuge at 100  $g$ . In both soils the normalised strength initially reduces before recovering cycle-by-cycle. The averaged values of  $s_u/s_{u-d}$  from the depth range analysed are plotted against cycle number ( $N$ ) in Fig. 2d. The ratio  $s_u/s_{u-d}$  approaches a value of unity after approximately 17 cycles for kaolin clay, suggesting the potential for full strength recovery, or a minimal impact of transient sensitivity due to irrecoverable inter-particle structure. The value for carbonate silt, however, is about 0.47–0.56 which indicates a partial recovery of the sensitivity. The sensitivity of carbonate silt is as much as twice that of the kaolin clay, yet the asymptotic value of  $s_u/s_{u-d}$  is half that of the kaolin clay, so it is highly likely that some inter-particle structure or “fabric” breaks down during the initial remoulding in the first packet of cycles, which cannot be recovered due to only dissipation of excess pore pressures under in-situ stress levels. This transient sensitivity is, crucially, not due to particle breakage because the tests performed using the same batch of carbonate silt material have shown that the initial sensitivity can be recovered via reconstitution, sedimentation and re-consolidation. The kaolin clay does not appear to exhibit the same transient sensitivity and almost all of the sensitivity is recoverable through re-consolidation without reconstitution and sedimentation.

Ideally, to properly model the influence of the changing strength of soils, a methodology is required that can capture the effects of near-undrained remoulding, consolidation induced volumetric hardening and recovery of clay sensitivity, and potentially strain rate-dependency. Analytical 1D frameworks proposed by White and Hodder (2010), Hodder et al. (2013), and Zhou et al. (2019) – implicitly allowing some recovery of the sensitivity due to consolidation – have been demonstrated to provide very good estimates of the varying strength when compared to T-bar penetrometer, such as that in Fig. 1. However, this aspect of soft clay behaviour has not found much attention in the field of numerical modelling, possibly due to the absence of a constitutive model allowing sensitivity regain, and issues related to mesh dependent strain localisation and scaling when classical continuum models such

as Finite Element Analysis (FEA) are applied to simulate problems involving strain-softening.

To investigate the remoulding and strain rate effects, Zhou and Randolph (2009) performed FE simulations of cycles of T-bar penetration in soft clay, using a simple Tresca-derived elastic-perfectly plastic constitutive model with strain-softening and strain rate effects proposed by Einav and Randolph (2005). In a more recent development, FE simulation of a cyclic T-bar penetration test involving undrained remoulding, consolidation, and subsequent consolidated-undrained T-bar resistance in kaolin clay was performed by Sabetamal et al. (2021) and Singh et al. (2021), using critical state based strain-softening–hardening constitutive models. Singh et al. (2021) demonstrated, by comparing numerically obtained results with the T-bar penetration test results, that the constitutive model adopted was unable to capture the second packet of strength degradation as well as the magnitude observed in T-bar experiments by Hodder et al. (2013) and O’Loughlin et al. (2020) due to the lack of regain in sensitivity. This is the case for most existing constitutive models, whether based on elastoplasticity such as S-CLAY1 (Wheeler et al., 2003), multi-laminate model for soft clay (Cudny and Vermeer, 2004), Saniclay (Dafalias et al., 2006), Modified Structured Cam Clay (Suebsuk et al., 2010), or hypoplasticity such as Hypoplastic Clay (Mašín, 2014), or viscoplasticity and viscohypoplasticity such as viscoplastic Saniclay (Rezania et al., 2016) and Viscohypoplastic Clay (Jerman and Mašín, 2020). This is primarily because such models were developed with a focus on capturing the typical soil response as observed in standard geotechnical element tests such as the triaxial test, where the magnitude of deformation applied to the sample is limited (shear strain  $\ll$  50%) such that a remoulded state is often not reached throughout the sample. Bjerre et al. (2018) proposed a constitutive model, SCA-R, for natural soft clays incorporating creep strain induced re-structuration. The authors are not aware of any attempt in the literature to develop a constitutive model allowing the consolidation induced (i.e. excess pore pressure driven) recovery of the sensitivity as observed in the penetrometer testing in reconstituted kaolin clay illustrated earlier.

The main objective of this paper is to develop a constitutive model that can capture the varying strength of fine-grained soils caused by strain rate dependency, remoulding and regain of sensitivity via re-consolidation in Large Deformation Finite Element (LD FE) framework. A viscoplastic strain-softening–hardening constitutive model based on classical Modified Cam Clay (MCC) (Roscoe and Burland, 1968) and Perzyana’s overstress theory (Perzyna, 1966) has been developed with a simple rule allowing consolidation induced recovery of the sensitivity via a link with the excess pore pressure dissipation. The integral-type non-local strain-softening approach was adopted to regularise the FE solutions, alleviating strain localisation issues and the model was implemented in the commercial FE software Abaqus, via its user-defined material subroutine UMAT. The model implementation is then validated by simulating constant strain rate triaxial compression and oedometer tests, comparing the numerical data with those derived from experiments. Finally, the model is applied to simulate cyclic T-bar penetrometer tests in normally consolidated (NC) and lightly over-consolidated (OC) kaolin clay, and NC carbonate silt (the experiments demonstrate degradation and recovery of strength sensitivity) via LD FE analyses using the Remeshing and Interpolation Technique with Small Strains (RITSS) (Hu and Randolph, 1998) methodology.

## 2. Viscoplastic Recoverable Sensitivity model (VRS model)

The VRS model is based on the Structured Modified Cam Clay (SMCC) constitutive model proposed by Mašín (2009), extended to incorporate strain rate effects using Perzyana’s overstress theory (Perzyna, 1966) and consolidation induced sensitivity recovery. The SMCC is an elastoplastic model based on classical modified cam clay that is capable of describing the strain-softening behaviour. Implementation of this model in LD FE modelling techniques, e.g. RITSS

scheme, is straightforward and has already been successfully performed by Singh et al. (2021). Therefore, this model was selected as a starting point for the development of a viscoplastic model that allows the prediction of strain-rate effects, strain-softening, and sensitivity recovery, with a small number of additional state variables in order to minimise the influence of the interpolation errors that occur in updated arbitrary Lagrangian–Eulerian large deformation modelling schemes.

### 2.1. Constitutive framework

The total strain rate in the overstress framework is assumed to be a sum of time-independent elastic and time-dependent viscoplastic strain components. Similar to the elastoplastic SMCC model, the time-independent elastic strain rate is obtained from isotropic elastic theory. The total strain rate  $\dot{\epsilon}$  can be given by:

$$\dot{\epsilon} = \dot{\epsilon}^e + \dot{\epsilon}^{vp} \quad (6)$$

where  $\dot{\epsilon}^e$  and  $\dot{\epsilon}^{vp}$  are elastic and viscoplastic strain rates, respectively. The stress rate  $\dot{\sigma}$  is linked to elastic strains via elastic stiffness matrix  $\mathbf{D}_e$  and can be written as:

$$\dot{\sigma} = \mathbf{D}_e : \dot{\epsilon}^e \quad (7)$$

The viscoplastic flow rule based on an overstress function is defined in order to derive a relationship between  $\dot{\epsilon}^{vp}$  and current stress state and the size of the yield surface. To achieve this, a static yield surface  $f$  identical to the yield surface of the SMCC model and a dynamic loading surface  $f_d$  (considered as a viscoplastic potential function) passing through the current stress state are defined (Perzyna, 1966), expressed respectively by:

$$f = q^2 + M^2 p' (p' - p_{cs}) = q^2 + M^2 p' (p' - p_{cs}) \quad (8)$$

and:

$$f_d = q^2 + M^2 p' (p' - p_{cd}) \quad (9)$$

where  $M$  is the gradient of the critical state line in  $p' - q$  space,  $p'$  and  $q$  are mean effective stress and deviatoric stress respectively, and the shapes of  $f$  and  $f_d$  are assumed to be identical but with different sizes controlled by the magnitudes of the  $p_{cs}$  and  $p_{cd}$  parameters, respectively (see Fig. 3). The quantity  $p_c$  is the size of the static yield surface for the reference soil with no sensitivity.

The viscoplastic strain rate can then be expressed assuming an associated flow rule with  $f_d$  as:

$$\dot{\epsilon}^{vp} = \mu_v \langle \phi(F) \rangle \frac{\partial f_d}{\partial \sigma} \quad (10)$$

in which  $\mu_v$  ( $\text{h}^{-1} \text{kPa}^{-1}$ ) is a fluidity parameter,  $\phi(F)$  is the overstress function representing the distance between  $f$  and  $f_d$ . The Macaulay brackets  $\langle \rangle$  are used to define the overstress function such that  $\langle \phi(F) \rangle = \phi(F)$  if  $F > 0$  and  $\langle \phi(F) \rangle = 0$  if  $F \leq 0$ . This means that the viscoplastic strains occur only when the stress state is outside the yield surface. In this work, the exponential form of overstress function (Yin et al., 2006; Yin and Hicher, 2008) is adopted giving:

$$\phi(F) = \left( \exp \left[ N_v \cdot \left( \frac{p_{cd}}{p_{cs}} - 1 \right) \right] - 1 \right) \quad (11)$$

where  $N_v$  is a viscosity parameter.

The model requires a total of twelve material parameters, which can be grouped into four distinct groups: (i) the basic parameters  $M$ ,  $\lambda^*$ ,  $\kappa^*$ ,  $N^*$  and  $v$ ; (ii) the strain-softening parameters  $k$ ,  $A$ ,  $S_t$ , and  $S_f$ ; (iii) the viscosity parameters  $\mu_v$  and  $N_v$ ; and (iv) the sensitivity recovery parameter  $R$ . The basic parameters have physical interpretations, as graphically presented in Fig. 4, that are consistent with the original Cam Clay model parameters, except that the so-called Butterfield compression law (Butterfield, 1979), relating the natural logarithm of the specific volume to natural logarithm of the mean effective stress ( $\ln(1+e) - \ln p'$ ) is favoured over the conventional  $e - \ln p'$  form. The

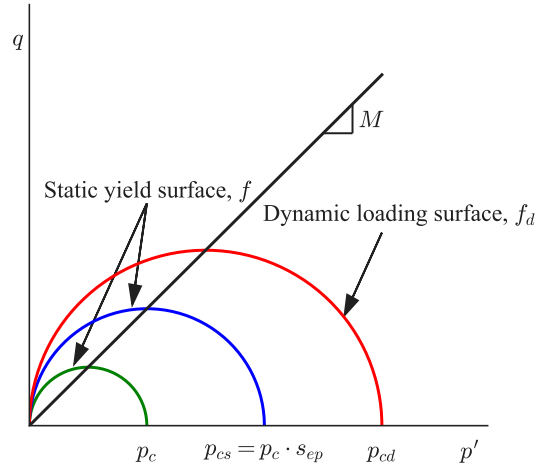


Fig. 3. Schematic representation of static yield surface  $f$  and dynamic loading surface  $f_d$  in VRS model.

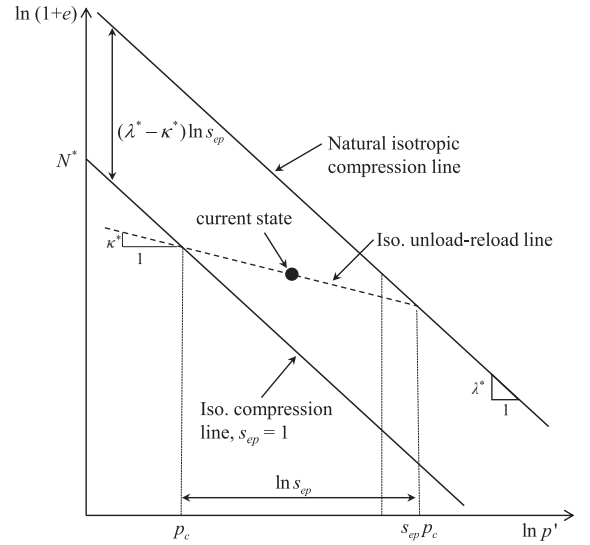


Fig. 4. Definitions of VRS model parameters  $N^*$ ,  $\lambda^*$ ,  $\kappa^*$ , sensitivity  $s_{ep}$  and quantity  $p_c$  at reference strain rate (identical to the parameters of the SMCC model by Mašin (2009)).

second group of parameters (to be defined later) control the strain-softening aspect of the model response. The third and fourth group of parameters govern the viscous and consolidation induced sensitivity recovery behaviour, respectively. The model has two state variables: void ratio  $e$  and sensitivity  $s_{ep}$ . The initial and final magnitudes of the sensitivity state variable  $s_{epi}$  and  $s_{epf}$  can be derived from the slopes of the normal consolidation line (NCL), unload-reload line (URL), the initial sensitivity  $S_t$ , and final sensitivity  $S_f$ , respectively, as follows:

$$s_{epi} = S_t^{(\lambda^*/(\lambda^* - \kappa^*))} \quad (12)$$

$$s_{epf} = S_f^{(\lambda^*/(\lambda^* - \kappa^*))} \quad (13)$$

The void ratio  $e$  is related to the quantity  $p_c$ , the size of the yield surface of the reference soil with  $s_{epi} = 1.0$ , through the following relationship:

$$\ln(1+e) = N^* - \kappa^* \ln p' - (\lambda^* - \kappa^*) \ln \left( \frac{p_c}{p_r} \right) \quad (14)$$

where  $p_r$  is a reference pressure, typically taken as 1 kPa.



The incremental strain rate drives the evolution of the state variables  $e$  and  $s_{ep}$  according to the following equations:

$$\dot{e} = -(1 + e)\dot{\epsilon}_v \quad (15)$$

$$\dot{s}_{ep} = -\frac{k}{(\lambda^* - \kappa^*)} (s_{ep} - s_{epf}) \dot{\epsilon}_{vs} + \dot{s}_{epr} \quad (16)$$

where  $k$  controls sensitivity degradation rate,  $s_{epf}$  is typically taken as unity,  $\dot{\epsilon}_v$  is volumetric strain rate,  $\dot{s}_{epr}$  is consolidation induced recovery rate of  $s_{ep}$ , which is controlled by the parameter  $R$ , and  $\dot{\epsilon}_{vs}$  is equivalent viscoplastic strain rate obtained from viscoplastic volumetric and deviatoric strain rates (i.e.,  $\dot{\epsilon}_v^{vp}$  and  $\dot{\epsilon}_q^{vp}$ , respectively), calculated as:

$$\dot{\epsilon}_{vs} = \sqrt{(1 - A) (\dot{\epsilon}_v^{vp})^2 + A (\dot{\epsilon}_q^{vp})^2} \quad (17)$$

As the local incremental plastic strains control the strain-softening response in this form of the model, mesh dependent FE solutions are obtained due to the strain localisation being linked to element size. To regularise the local FE analyses, an integral type non-local softening method (Bažant and Jirásek, 2002) is applied. In this approach, the strain-softening response at a material point is linked to the state of plastic deformation not only at that point but also at the neighbouring material points. The numerical implementation details of the methodology are presented in Singh et al. (2021). In brief, the approach simply uses a spatially weighted measure of the volumetric and deviatoric strains,  $\dot{\epsilon}_v^{vp}$  and  $\dot{\epsilon}_q^{vp}$ , to control the softening response, similar to Galavi and Schweiger (2010), Summersgill (2014), Mánica et al. (2018), and Monforte et al. (2019). In the local VRS model, the generalised viscoplastic strain given by Eq. (17) drives the strain-softening response at an FE integration point (IP). In the non-local VRS model, this value is replaced by a spatially averaged value of the same quantity, where the size of the averaging zone and weighting is controlled through the parameter  $l_c$  typically referred to as the ‘characteristic length’ which adds a length scale dependency into the constitutive response to indirectly govern the size of the strain localisation features (or shear bands).

## 2.2. Implementation of recoverable sensitivity

The behaviour of different clays exhibiting different degrees of sensitivity is commonly attributed to varying inter-particle structure in the consolidated soil (or ‘fabric’) and bonding. According to Cotecchia and Chandler (2000), the structure resulting from the geological history of the clay can be divided into two categories: sedimentation and post-sedimentation structure. The sedimentation structure includes all structure that develops solely due to the one-dimensional consolidation process, and is present in normally consolidated natural and reconstituted clays. The post-sedimentation structure, however, develops due to some geological intervention after normal consolidation in the form of mechanical unloading, long term processes such as creep, thixotropy, and post-deposition bonding. This study considers only the recovery of sensitivity due to primary consolidation induced structure. Based on the experimental data presented earlier, it is assumed in formulating the recovery framework that the development of the excess pore pressures during undrained remoulding of the clay causes degradation of strength and thus sensitivity, and dissipation of those excess pore pressures leads to a degree of recovery of the sensitivity. This sensitivity recovery,  $\dot{s}_{ep}$  in incremental form, is linked to the dissipation of the excess pore pressures via volumetric strains  $\dot{\epsilon}_v$  for simplicity and straightforward numerical implementation in LDFE modelling, and is expressed as:

$$\dot{s}_{ep} = -\frac{\langle R s_{epi} - s_{ep} \rangle}{\left( \frac{\lambda^* - \kappa^*}{\lambda^*} \right) \kappa^* \ln \left( \frac{s_{epi}}{s_{ep}} \right)} \ln (1 - \langle \dot{\epsilon}_v \rangle) \quad (18)$$

in which  $s_{ep}$  is the current value of the sensitivity state variable,  $R$  is a parameter that controls the fraction of the initial sensitivity

recoverable due to re-consolidation, and  $\dot{\epsilon}_v$  is the volumetric strain rate. The Macaulay brackets in the numerator of Eq. (18) ensure that the recovery occurs only when  $s_{ep}$  is less than  $R s_{epi}$  and compressive volumetric strains develop.

Fig. 5 illustrates the recovery framework through the idealised effective stress path of a rate-independent soil element in  $\ln(1+e)-\ln p'$  space subjected to undrained shearing from an isotropically consolidated state, and subsequent consolidation and undrained shearing events. In remoulding of an NC soft clay, the magnitude of the excess pore pressure required to generate an apparent sensitivity of  $S_t$  (i.e. a fully remoulded state) can be approximated to be equal to the horizontal separation of the isotropic compression lines (ICL) for  $s_{ep} = s_{epi}$  and  $s_{ep} = s_{epf}$ , along a constant void ratio line (i.e. the black solid line passing through ABC in Fig. 5a and b), with the fully remoulded soil state reached (at C) as the yield surface collapses to its minimal size.

Re-consolidation and subsequent undrained shear stress paths are presented for the cases of no recovery ( $R = 0$ ), full sensitivity recovery potential ( $R = 1$ ), and partial recovery of the sensitivity ( $s_{epf}/s_{epi} < R < 1$ ). In both Fig. 5a and b, the red dashed and solid lines represent a range of re-consolidation and subsequent undrained shear paths for the case of no sensitivity recovery ( $R = 0$ ). The dashed and solid blue lines in Fig. 5a and b represent a range of possible re-consolidation and subsequent undrained shear stress paths, respectively, for full and partial sensitivity recovery. The conventional form of the model,  $R = 0$ , does not allow  $s_{ep}$  to increase above  $s_{epf}$  during consolidation; therefore, the stress state can just reach the ICL for the remoulded soil (i.e.  $s_{ep} = s_{epf}$ ), and any further increase in  $p'$  would occur along the ICL (see stress path C  $\rightarrow$  D  $\rightarrow$  I  $\rightarrow$  K in Fig. 5a and b), increasing the size of the yield surface through plastic volumetric hardening.

Eq. (18) with  $R > 0$  allows the stress state during consolidation to cross over to the right of the ICL for  $s_{ep} = s_{epf}$  due to incremental recovery of sensitivity. Dissipation, along a URL, of the same magnitude of excess pore pressure required to realise a sensitivity of  $S_t$  in undrained shear, induces a volumetric compression of  $\kappa^* \ln(S_t)$  or  $((\lambda^* - \kappa^*)/\lambda^*) \ln(s_{epi}/s_{epf})$ , leading to recovery of the sensitivity  $S_t$  or state variable  $s_{ep}$  from  $s_{epf}$  to  $s_{epi}$  for  $R = 1$ . This is illustrated by the stress path C  $\rightarrow$  D  $\rightarrow$  E in Fig. 5a and b for full ( $R = 1$ ) and partial recovery of the sensitivity (i.e.  $R < 1$ ), respectively. Following recovery of the sensitivity state variable to a state where  $s_{ep} = R s_{epi}$ , the stress paths follow the ICL, again increasing the size of the yield surface through plastic volumetric hardening through the stress paths E  $\rightarrow$  G in Fig. 5a and b for full and partial sensitivity recovery, respectively. The case with  $R = 1$  clearly has the capacity to generate more excess pore pressure in subsequent undrained shear (stress path G  $\rightarrow$  H in Fig. 5a and b) due to the greater degree of recovered sensitivity allowed on dissipation of excess pore pressures. It is also apparent from this simple model that for the same magnitude of excess pore pressure dissipation, the variants with sensitivity recovery ( $R > 0$ ) experience less volumetric compression (c.f. E  $\leftrightarrow$  I and G  $\leftrightarrow$  K in Fig. 5a and b).

The strength variation factor,  $s_u/s_{u-d}$ , extracted from an episodic T-bar penetration test as demonstrated in Fig. 2, indicates the potential amount of excess pore pressure that can be generated in repeated undrained cyclic deformation of the soil; thus, the potential recoverable amount of the sensitivity due to re-consolidation can be given by  $(s_u/s_{u-d}) \cdot S_t$ . The recovery parameter  $R$  can therefore be estimated from the measured  $s_u/s_{u-d}$  using the following equation, derived based on the relationship between sensitivity,  $S_t$ , and initial value of the sensitivity state variable,  $s_{epi}$ , given by Eq. (12):

$$R = \frac{\left( \left( \frac{s_u}{s_{u-d}} \right) \cdot S_t \right)^{\left( \frac{\lambda}{\lambda - \kappa} \right)}}{S_t^{\left( \frac{\lambda}{\lambda - \kappa} \right)}} = \left( \frac{s_u}{s_{u-d}} \right)^{\left( \frac{\lambda}{\lambda - \kappa} \right)} \quad (19)$$

Fig. 6 illustrates the evolution of the sensitivity state variable  $s_{ep}$  for cyclic undrained shear with re-consolidation to a consistent mean stress  $p'$  after each remoulding cycle. The sensitivity state variable  $s_{ep}$

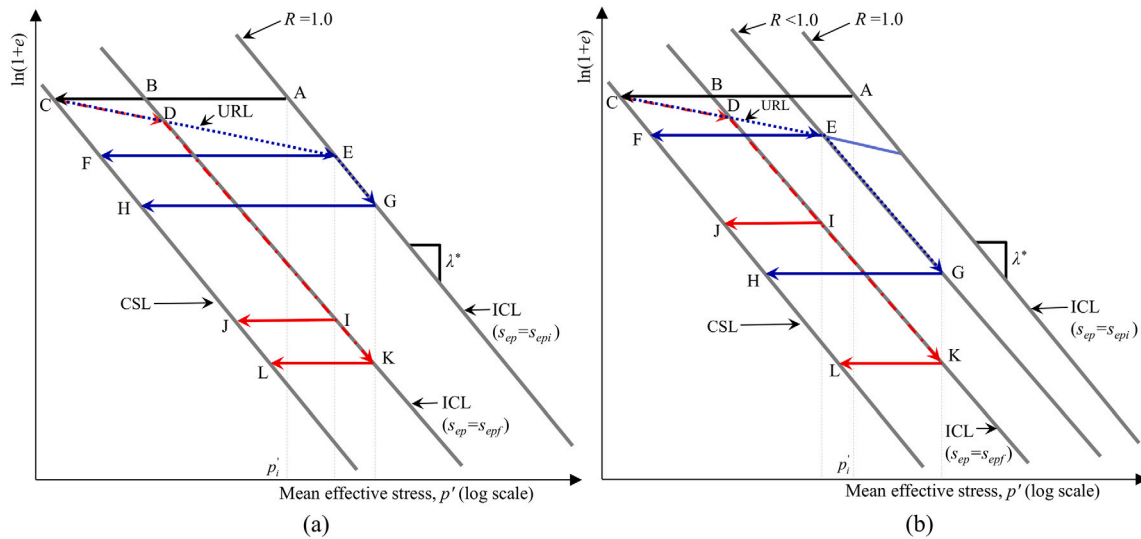


Fig. 5. Effective stress paths in  $\ln(1+e) - \ln p'$  space during undrained shearing, consolidation, and consolidated-undrained shearing with potential of: (a) full sensitivity recovery, and (b) partial sensitivity recovery.

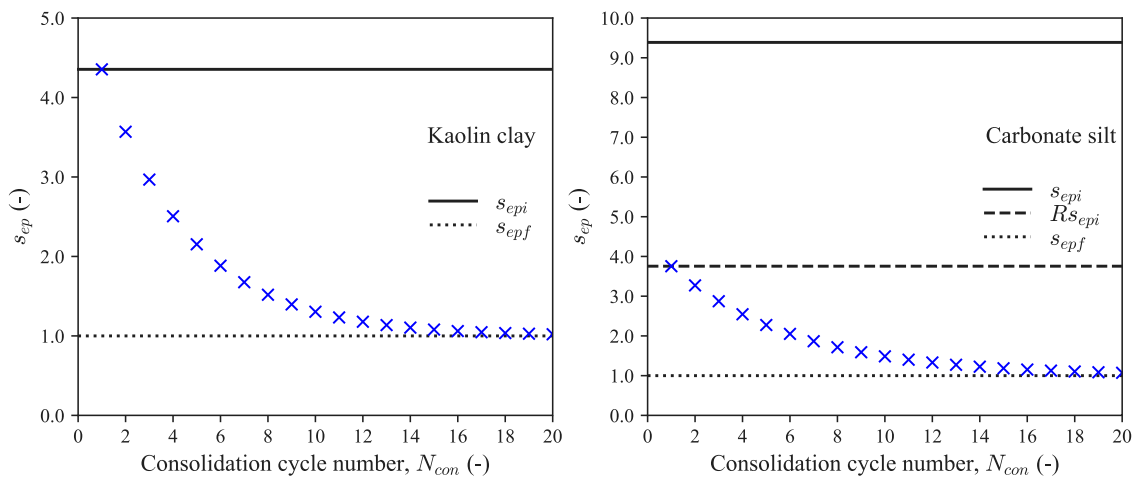


Fig. 6. Evolution of the sensitivity state variable  $s_{ep}$  as per Eq. (18) for cyclic undrained shear with re-consolidation to a consistent mean stress  $p'$  after each remoulding cycle: (a) full sensitivity recovery, and (b) partial sensitivity recovery.

will eventually tend to unity, which is a true residual state with no generation of excess pore pressure under continuous constant volume shear. Fig. 6a and b simulate the evolution of the sensitivity state variable for the kaolin clay and carbonate silt shown in Fig. 2, respectively, illustrating the effect of the partial recovery of sensitivity in the case of the carbonate silt.

### 2.3. Numerical implementation

The VRS model has been implemented in the commercial FE code Abaqus through its user material subroutine, UMAT. The time integration is performed using a step-by-step semi-implicit integration scheme proposed by Katona (1984) and recently successfully applied in boundary value problem simulations by Rezaian et al. (2016). A second time integration approach, based on a modified Euler sub-stepping algorithm with error control adopted by Kelln et al. (2008) to implement their viscoplastic constitutive model in FE solutions, was also incorporated in the user subroutine for a comparison of the two integration schemes to establish the validity of the integration scheme. A sub-stepping scheme which allows application of the whole strain increment in parts was adopted in both Katona and Kelln's algorithms. The local sub-step size

for the current iteration was controlled based on the rate of the convergence in the previous sub-step ensuring a computationally efficient implementation. Both the methodologies produced stable responses in element test and boundary value problem simulations. 'Kelln's method' was found to be more computationally efficient in the cyclic T-bar simulations and was adopted in all the analyses.

### 3. Model validation

Validation of the VRS model was carried out by simulating several constant strain rate oedometer tests on St. Herblain clay and undrained triaxial compression tests on Haney clay using the user material subroutine implemented in Abaqus. The CRS oedometer test data for St. Herblain clay were reported in Rangeard et al. (2002), Yin et al. (2010), Rezaian et al. (2016), and Jerman and Mašin (2020). The triaxial compression tests on Haney clay were performed by Vaid and Campanella (1977) and are documented in Vermeer and Neher (1999) and Rezaian et al. (2016).

#### 3.1. CRS oedometer tests on St. Herblain clay

Constant strain rates oedometer test were simulated and the results obtained were compared against the experiments performed on St.

**Table 1**  
Parameters for St. Herblain clay and Haney clay.

Parameter	St. Herblain clay	Haney clay	Unit
Slope of NCL, $\lambda^*$	0.145	0.0684	–
Slope of RCL, $\kappa^*$	0.0098	0.0113	–
Poisson's ratio, $\nu$	0.3	0.25	–
Frictional constant, $M$	1.25	1.28	–
Intercept of the NCL at $p' = 1$ kPa, $N^*$	1.69	1.78	–
Initial sensitivity, $S_i$	1.0	4.46	–
Final sensitivity, $S_f$	1.0	1.0	–
Degradation rate, $k$	0.0	0.1	–
Degradation ratio, $A$	0.0	0.3	–
Fluidity parameter, $\mu_v$	$1.8 \times 10^{-5}$	$4.14 \times 10^{-6}$	$\text{h}^{-1} \text{ kPa}^{-1}$
Viscosity exponent, $N_v$	9.0	15.0	–
Sensitivity recovery parameter, $R$	0.0	0.0	–

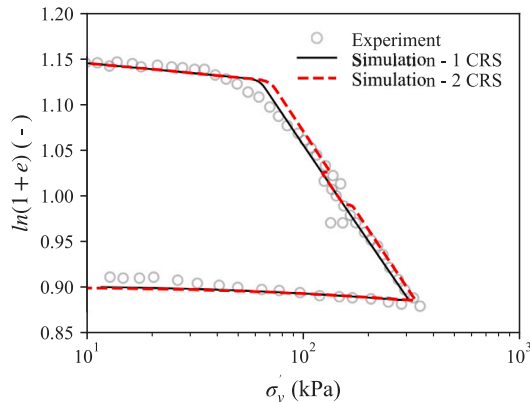


**Fig. 7.** Experimental and numerical simulation data of oedometer test on St. Herblain clay at a constant rate of strain of  $2.37 \times 10^{-3}/\text{h}$  (1 CRS) and  $1.18 \times 10^{-2}/\text{h}$  -  $2.37 \times 10^{-3}/\text{h}$  (2 CRS).

Herblain clay. The test involved two strain rates — first 12% vertical strain was applied with  $\dot{\epsilon}$  of  $1.18 \times 10^{-2}/\text{h}$ , and then 12% to 15.5% vertical strain with  $\dot{\epsilon}$  of  $2.37 \times 10^{-3}/\text{h}$ , and the remaining again with the initial strain rate. In this comparison, the reference strain rate was considered as  $2.37 \times 10^{-3}/\text{h}$  and the basic model input parameters ( $\lambda^*$ ,  $\kappa^*$ , and  $N^*$ ) were calibrated by optimising numerically obtained vertical stresses against the experimentally obtained response (see black solid line in Fig. 7). The viscosity parameters are similar to those adopted in Rezaei et al. (2016) as both viscoplastic Saniclay and the current model employ an identical over-stress function. The remaining parameters,  $M$  and  $\nu$ , were taken from Rezaei et al. (2016). The model parameters adopted are listed in Table 1. The red dashed line in Fig. 7 is numerically obtained vertical stresses for the test with two constant strain rates. The model captures the major features of the experiment including the variation of vertical stresses due to varying strain rate.

### 3.2. Undrained triaxial tests on Haney clay

In this section, the numerically obtained response of undrained triaxial compression tests on Haney clay is compared with the tests presented in Vaid and Campanella (1977). The samples used in these tests were initially consolidated under an isotropic cell pressure of 525 kPa for 36 h and were allowed to stand for 12 h under undrained conditions before shearing the sample. The preconsolidation pressure just before shearing was found to be 373 kPa. The model input parameters were taken from Rezaei et al. (2016) and are listed in Table 1. In the absence of oedometer test data, the basic model parameters  $\lambda^*$  and  $\kappa^*$  were obtained by converting the values derived by Rezaei et al. (2016) for the Saniclay model in  $e - \ln \sigma'_v$  space to the Butterfield compression law adopted in the current model in  $\ln(1+e) - \ln p'$  space. The best

values of the strain softening and the viscosity parameters were selected by trial and error. The model parameters adopted are listed in Table 1. The results obtained from the simulations with several axial strain rates are compared with the tests and are presented in Fig. 8. The predicted deviator stress-axial strain responses for the strain rates of 0.0094%/h, 0.15%/h, and 1.15%/h are in good agreement with those observed from the tests (see Fig. 8a). The maximum value of deviator stress is plotted against the strain rate in Fig. 8b. The value increases linearly with increasing strain rate and is very close to the experimentally obtained values for all strain rates.

## 4. Numerical simulation: T-bar penetrometer tests

As illustrated earlier, the changing strength of soils due to strain-softening and re-consolidation can be investigated using an episodic cyclic T-bar penetration test with dissipation periods between the undrained cyclic penetration episodes. In this paper, similar T-bar tests performed on soft kaolin clay and carbonate silt in a single gravity setup and a geotechnical centrifuge (Hodder et al., 2013; O'Loughlin et al., 2020) have been simulated using the VRS model in LDFE analyses to demonstrate its capabilities in capturing the varying strength due to remoulding and re-consolidation. Hodder et al. (2013) performed the T-bar penetrometer tests in lightly over-consolidated kaolin clay using a model T-bar of 5 mm diameter ( $D$ ) (i.e. equal to 0.25 m in prototype scale at 50 g in the centrifuge). The test simulated here was performed at 50 g in the UWA small beam centrifuge, and consisted of three episodes of 20 T-bar cycles carried out at a penetration rate of 1 mm/s, with re-consolidation periods between the cyclic penetration episodes. The non-dimensional penetration rate  $v/D$  was  $7.2 \times 10^4 \text{ %/h}$ . Tests with a similar sequence were carried out by O'Loughlin et al. (2020) in normally consolidated kaolin clay and carbonate silt samples at single gravity and 150 g levels in the same facility. A 5 mm diameter T-bar (i.e. equal to 0.75 m in prototype scale at 150 g in the centrifuge) with a penetration velocity  $v$  of 3 mm/s was used in the undrained displacement cycles, leading to a nominal strain rate  $v/D$  of  $1.44 \times 10^5 \text{ %/h}$ . The kaolin samples used in the single gravity experiments were normally consolidated to a stress level of 48 kPa, whereas the high gravity samples were normally consolidated in the centrifuge under self-weight. Dissipation periods of 1 and 2.5 h in the centrifuge tests were included between the undrained cyclic episodes for the kaolin clay and carbonate silt, respectively, which had been calculated to be sufficient for full dissipation to occur. Given the drainage path length was the same in single gravity tests as it was in the centrifuge — since the scale factor for consolidation time is 1 (Garner et al., 2007) and the same penetrometer was used for all tests — it would also have been sufficient for the laboratory floor tests. However, a 24 h period was used for the single gravity tests in order to ensure full dissipation had indeed occurred in the centrifuge experiments, which was confirmed. Hence, in all cases the dissipation time between penetration cycles was sufficient to facilitate full dissipation of excess pore pressure generated by the previous packet of undrained cycles, yet sufficiently short that effects due to long-term creep or ageing would be minimal.

### 4.1. Model parameters

The model input parameters for the UWA kaolin clay and carbonate silt adopted in this study are listed in Table 2. The basic parameters were adopted from Ragni et al. (2015) and Chow et al. (2019). The T-bar test derived sensitivities ( $S_{T-bar}$ ) of kaolin and carbonate silt are 2.2–2.5 and 5.0, respectively, but as demonstrated by Zhou and Randolph (2009) and Singh et al. (2021), a value of initial sensitivity,  $S_i$ , higher than  $S_{T-bar}$  is required in cyclic T-bar simulations to obtain a numerical model response that matches with the test results. Therefore, due to the difficulties in calibration of the softening parameters using standard geotechnical element tests (such as triaxial compression), as highlighted by Singh et al. (2021), the softening parameters ( $S_i$ ,  $k$

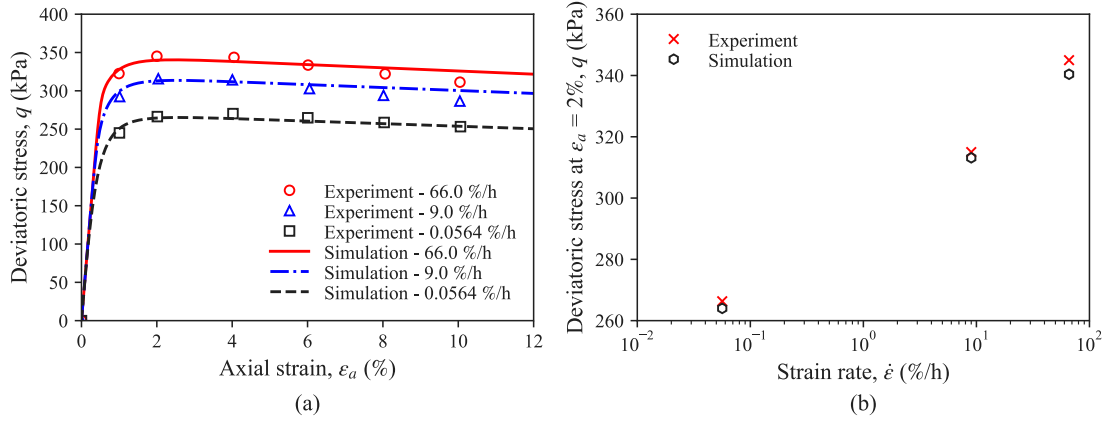


Fig. 8. Experimental and numerical simulation data of undrained triaxial compression tests on Haney clay at a constant rate of strain (a) deviator stress  $q$  against axial strain  $\epsilon_a$  and (b) deviator stress  $q$  at axial strain of 2% against strain rate  $\dot{\epsilon}$ .

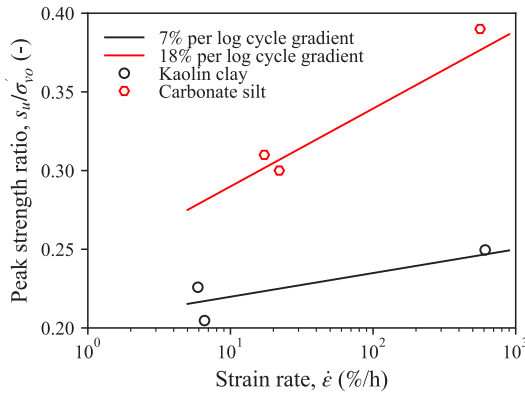


Fig. 9. Experimental data of constant rate simple shear testing of kaolin clay and carbonate silt using 'UWA type' apparatus: peak undrained strength ratio  $s_u/\sigma'_{v0}$  against strain rate  $\dot{\epsilon}$ .

and  $A$ ) were identified by best fitting the numerically obtained cyclic strength degradation response of the first undrained episode to the results of the experiment. The non-local regularisation parameter, the characteristic length ( $l_c$ ), was assumed to be 0.01 m in all of the analyses. This value was selected by considering the size of the coarsest mesh element size in the soil full-flow failure zone, and ensuring the characteristic length was at least twice as large.

The strain rate dependency responses of kaolin clay and carbonate silt are presented in Fig. 9, plotting the results of direct simple shear (DSS) tests performed on kaolin clay (Reid, 2021) and carbonate silt (Guevara et al., 2022) using the 'UWA type' simple shear apparatus. The peak undrained strength ratio  $s_u/\sigma'_{v0}$  is plotted against the strain rate  $\dot{\epsilon}$ . The data points were best fitted with 7% and 18% increases per log cycle of  $\dot{\epsilon}$ , respectively. The viscoplastic strain rate  $\dot{\epsilon}^{vp}$  in the VRS model is determined using Eq. (10) in which the viscous parameters  $\mu_v$  and  $N_v$  influence both the strain rate dependency of the strength and the reference strain rate. As explained by Yin et al. (2006), the parameter  $\mu_v$  controls the reference strain rate (i.e. the strength at this strain rate is the reference strength), and the parameter  $N_v$  governs the rate dependent strength enhancement. These parameters can be obtained either from CRS oedometer tests, conventional oedometer tests or in situ tests as described by Yin and Hicher (2008) and Yin et al. (2010). In the absence of long term experimental data, the parameters  $\mu_v$  and  $N_v$  for kaolin clay and carbonate silt were selected from single element undrained simple shear simulations, assuming the reference  $\dot{\epsilon}$  of 1%/h and the undrained strength enhancement of 7% and 18% for every log cycle increase in  $\dot{\epsilon}$ .

Table 2

Parameters for UWA kaolin clay and carbonate silt.

Parameter	Kaolin clay	Carbonate silt	Unit
Slope of NCL, $\lambda^*$	0.0811	0.0913	–
Slope of RCL, $\kappa^*$	0.019	0.016	–
Poisson's ratio, $\nu$	0.3	0.3	–
Frictional constant, $M$	0.90	1.62	–
Intercept of the NCL at $p' = 1$ kPa, $N^*$	1.195	1.408	–
Initial sensitivity, $S_i$	3.08	6.35	–
Final sensitivity, $S_f$	1.0	1.0	–
Degradation rate, $k$	0.02	0.06	–
Degradation ratio, $A$	0.2	0.1	–
Fluidity parameter, $\mu_v$	$3.6 \times 10^{-4}$	$2.52 \times 10^{-4}$	$\text{h}^{-1} \text{ kPa}^{-1}$
Viscosity exponent, $N_v$	20.0	10.0	–
Sensitivity recovery parameter, $R$	1.0	0.4–0.5	–

The simulation results are shown in Fig. 10 for kaolin clay, varying  $\mu_v$  and the strain rate  $\dot{\epsilon}$ . The deviatoric stress  $q$  normalised by its reference value  $q_{ref}$  is plotted against  $\mu_v$  and  $\dot{\epsilon}$  for  $N_v$  of 10.0 and 20.0. It can be seen that  $q/q_{ref}$  increases with a decrease in  $\mu_v$ , with  $q/q_{ref}$  assuming a value of unity for  $\mu_v$  greater than  $3.6 \times 10^{-4} \text{ h}^{-1} \text{ kPa}^{-1}$  for the analyses with  $N_v$  of 10.0 and 20.0. An almost linear enhancement of about 13% and 7% in  $q/q_{ref}$  is observed per log cycle increase in strain rate for  $N_v = 10.0$  and 20.0 respectively. Similarly, the values of  $\mu_v$  and  $N_v$  were selected for carbonate silt using the same approach. The adopted values are given in Table 2.

#### 4.2. LDFE modelling details

A two dimensional plane strain T-bar of  $D = 0.04$  m diameter T-bar was simulated, with the FE analysis mesh shown in Fig. 11. Due to the symmetrical geometry of the problem, only half of the problem domain was modelled for computational efficiency. The T-bar was assumed to be 'wished-in-place' with an initial embedment of  $5.5D$  and the horizontal and vertical extents of the soil region mesh were taken as  $10D$  and  $15D$ , respectively. To minimise the propagation of interpolation errors in the stress state and state variables caused by repeated remeshing, a partial remeshing scheme was adopted where only the near-field region (i.e. close to the T-bar) was periodically remeshed following Zhou and Randolph (2009) and Singh et al. (2021). The remeshing region comprises very fine elements near to the T-bar and then gradually transitions into a coarse mesh in the non-remeshing far field (see Fig. 11). The T-bar-soil surface interaction was assumed to be smooth with normal separation restricted (i.e. smooth no breakaway).

Similar to the single gravity experiments, which involved a consolidation stress of 48 kPa, the initial normally consolidated soil state in all the analyses was achieved by applying a surcharge pressure of 50 kPa



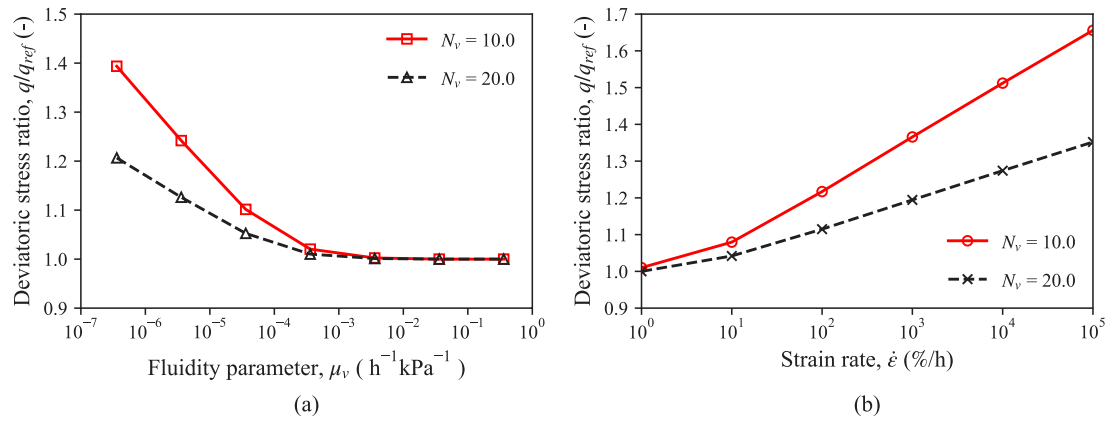


Fig. 10. Selection of viscous parameters  $\mu_v$  and  $N_v$  for kaolin clay from: (a)  $q/q_{ref}$  -  $\mu_v$ , and (b)  $q/q_{ref}$  -  $\dot{\epsilon}$ , respectively.

at the top boundary of the mesh, giving approximately uniform soil strength with depth, and the ‘correct’ vertical and horizontal stresses were applied as an initial stress condition throughout the soil domain. The value of lateral coefficient of earth pressure at rest,  $K_0$ , was considered equal to  $1 - \sin(\phi_c)$ , where  $\phi_c$  is the critical state effective friction angle of the soil. The permeability  $k_s$  was taken as  $1 \times 10^{-9}$  m/s and  $1.64 \times 10^{-9}$  m/s for kaolin and carbonate silt, respectively.

Displacement controlled analyses were performed to obtain the cyclic penetration response, with velocities of 24 mm/s for the cases of NC kaolin clay and carbonate silt and 8 mm/s for OC kaolin clay, which were obtained from the operative  $v/D$  in the T-bar experiments to which the simulations are compared. The T-bar was penetrated by  $4D$  from the initial position in the first penetration cycle to partially remould the soil, establishing a steady-state penetration condition. Penetration cycles with  $3D$  amplitude were carried out until a fully remoulded asymptotic state was achieved. The mesh used eight-noded bi-quadratic plane strain quadrilateral, reduced integration elements (CPE8R in the Abaqus Standard library) for the undrained penetration cycles. To perform consolidation analyses, eight-noded plane strain quadrilateral, bi-quadratic displacement, bi-linear pore pressure, reduced integration elements (CPE8RP in the Abaqus Standard library) were used to discretise the soil domain. The undrained stress-strain soil response was described by adding the bulk modulus of the pore water to the effective stress-strain matrix in an Abaqus ‘static’ step. The soil state at the end of undrained cycles was mapped to a coupled pore-fluid effective stress analysis (an Abaqus ‘soils’ step) to allow the dissipation of the excess pore pressures to be simulated. During the dissipation process, the T-bar was parked at the bottom of the remoulded zone (i.e.  $z/D = 9.5$  in Fig. 11). The undrained cycle following the consolidation step was again considered as a ‘static’ step by augmenting the effective stress-strain matrix once again with the bulk modulus of water. This methodology improved the analysis convergence compared to a purely fully-coupled strategy.

The actual penetrometer tests by Hodder et al. (2013) and O’Loughlin et al. (2020) comprised three packets of 20 cycles of undrained T-bar penetration, with dissipation periods between each episode. However,  $\approx 95\%$  strain softening occurred in the first five cycles, and therefore only the first five cycles of the first episode are simulated in this paper for computationally efficient analyses and to minimise the impact of interpolation errors that are inevitable due to the frequent remeshing required. After this, a dissipation analysis and one cycle of consolidated-undrained penetration was performed. The analyses were carried out using the VRS model with  $R = 0$  (no recovery of sensitivity) and  $R > 0$  (i.e. with some recovery of sensitivity).

#### 4.3. T-bar twitch penetration test: an alternative method of estimating model viscosity parameters

In the viscous region of clay behaviour ( $vD/c_v > 30$ ), the undrained penetration resistance of an advancing penetrometer decreases with

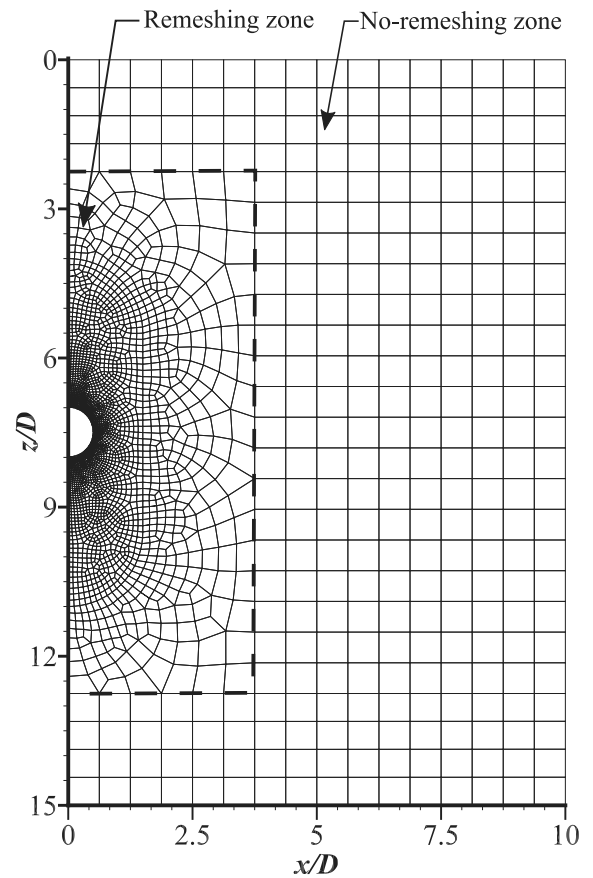


Fig. 11. Illustration of the initial FE analysis mesh used for the cyclic T-bar simulations as adopted in Singh et al. (2021).

a reduction in strain rate due to the development of higher excess pore pressures at slower strain rates. On further decrease in the strain rate, the response transitions from undrained to the partially drained regime, leading to higher penetration resistance. Therefore, a single penetrometer twitch or variable rate penetration test can successfully be used to generate a backbone curve relating the resistance with the penetration rate, investigating both viscous and consolidation aspects of the behaviour (House et al., 2001; Randolph, 2004; Chung et al., 2006). In this section, a variable rate T-bar test was simulated and compared against the constant rate T-bar test simulation. The T-bar was advanced by a total of  $4D$  displacement from the initial position with  $1D$  penetration with each strain rate of 24, 12, 1, and 0.1 mm/s, and

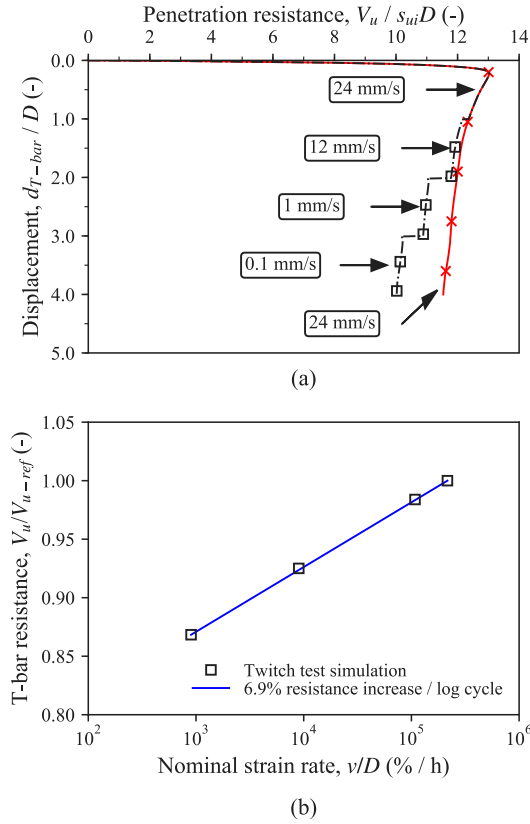


Fig. 12. Results of T-bar monotonic and twitch tests simulation: (a) penetration resistance profile, and (b) normalised T-bar resistance against normalised velocity or nominal strain rate.

the obtained results are presented in Fig. 12. The penetration resistance normalised by intact strength at the reference strain rate of 1%/h and T-bar diameter ( $V_u/s_{ui}D$ ) is plotted against normalised displacement ( $d_{T-bar}/D$ ) in Fig. 12a. Fig. 12b presents the T-bar resistance at the midpoint of every 1D displacement normalised by the constant/reference rate (24 mm/s) resistance at the corresponding depth  $V_u/V_{u-ref}$ , plotted against the nominal strain rate  $v/D$ . The penetration resistance decreases by about 7% for every log cycle decrease in  $v/D$ , which is in a very good agreement with the expected value based on the simple shear analyses illustrated earlier in Fig. 9. The analysis demonstrates the robustness of implementation of the constitutive model via an LDFE analysis, and shows that the viscosity parameter  $N_v$ , therefore, can directly be identified from a twitch penetration test.

#### 4.4. Results: T-bar cycling in kaolin clay

##### 4.4.1. Normally consolidated conditions

The results obtained from numerical simulations of T-bar cycles in NC kaolin clay are plotted in Fig. 13 for the cases of  $R = 0$  and  $R = 1$ . Fig. 13a shows penetration resistance normalised by the T-bar diameter and intact shear strength at a reference strain rate of 1%/h ( $V_u/s_{ui}D$ ) plotted against normalised displacement ( $d_{T-bar}/D$ ). Fig. 13b presents the numerically obtained penetration resistance variation factor ( $V_u/V_{u-ref}$ ) at the mid of the T-bar cycling zone (i.e.  $d_{T-bar}/D$  of 2.5) plotted against the penetration cycle number ( $N$ ), referring to the first pass as cycle number  $N = 0.25$  following the convention suggested by Randolph et al. (2007) and Zhou and Randolph (2009). The results extracted from the cyclic T-bar penetration test in kaolin clay are also presented in the figure with pentagonal and hexagonal markers. The normalised resistance first mobilises a peak value in the initial penetration before degrading rapidly to a steady value with further

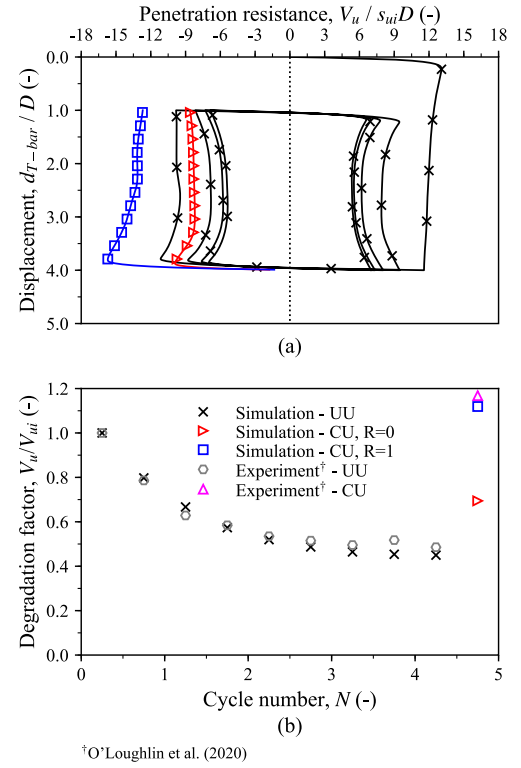
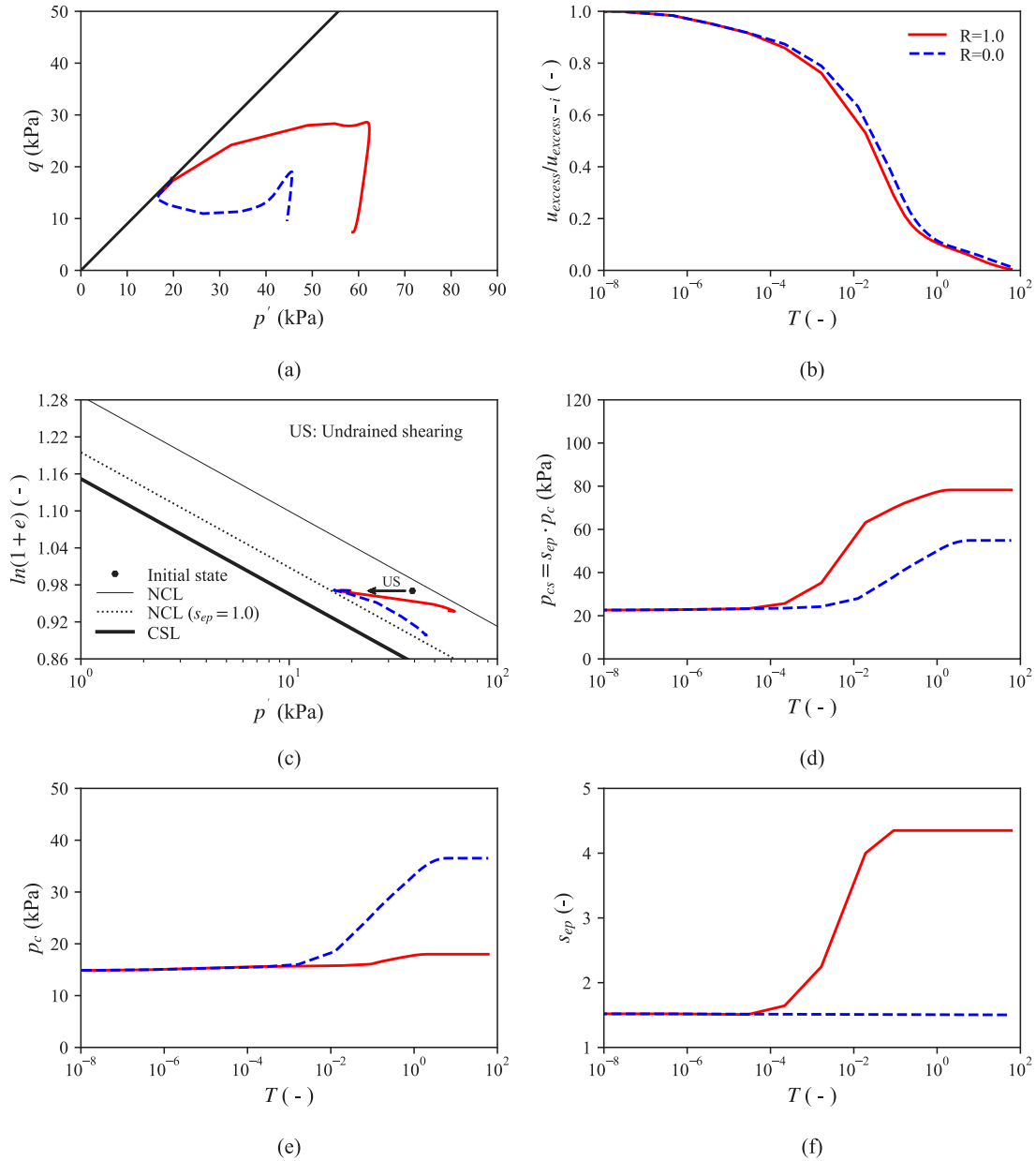


Fig. 13. Cyclic undrained and consolidated-undrained T-bar penetration in NC kaolin clay: (a) penetration resistance, and (b) strength degradation factor.

advancement, and a very close match between the resistance variation factors  $V_u/V_{u-ref}$  obtained from the simulation and the experiment is obtained (Fig. 13b). The recovery parameter only influences behaviour post-consolidation, thus the UU (undrained penetration) response for  $R = 0$  and  $R = 1$  cases are identical, and therefore only one data set is plotted for visual clarity. Post re-consolidation, only a single pass of undrained penetration was performed to obtain the CU (undrained penetration post re-consolidation) T-bar resistance for the two analyses. The results obtained are shown in the Fig. 13 as a red solid line with triangular markers ( $R = 0$ ) and a blue solid line with square markers ( $R = 1$ ). The penetration resistances increased by about 1.68 and 2.49 times for  $R = 0$  and 1, respectively compared to the remoulded resistances observed at the end of the remoulding cycles. The value extracted from the experiment is 2.8, which is about 12 and 67% higher than the values obtained from the sensitivity recovery and no-recovery analyses, respectively.

Fig. 14 presents the re-consolidation response as stress paths in  $p'-q$  and  $\ln(1+e)-p'$  spaces, dissipation history, and the evolution of other state variables with time for the soil element immediately beneath the T-bar invert with blue dashed and red solid lines for the analyses with  $R = 0$  and  $R = 1$ , respectively. The contours of the current undrained shear strength  $s_u$  normalised by the intact undrained shear strength  $s_{ui}$  are shown in Fig. 15 for the soil states following remoulding and re-consolidation. The undrained shearing causes development of the excess pore pressures ( $u_{excess}$ ), resulting in a decrease in  $p'$  from the in situ state at a constant void ratio  $e$  (see arrow US in Fig. 14c). During dissipation, the effective stresses  $p'$  increase, with a higher increase in  $p'$  and a lesser decrease in void ratio  $e$  for the case with  $R = 1$  due to recovery of the sensitivity resulting in a stronger soil. The dissipation histories of the excess pore pressure normalised by its initial value ( $u_{excess}/u_{excess-i}$ ) plotted against dimensionless time ( $T$ ) obtained from the two analyses are very similar (see Fig. 14b). The dimensionless time  $T$  is expressed by:

$$T = \frac{c_v t}{D^2} \quad (20)$$



**Fig. 14.** Re-consolidation response of NC kaolin element beneath T-bar invert: (a) stress path in  $p'$  -  $q$  space, (b) normalised excess pore pressure  $u_{\text{excess}}/u_{\text{excess}-i}$  against dimensionless time  $T$ , (c) stress path in  $\ln(1+e)$  -  $p'$  space, (d) static yield surface size  $p_{cs}$  against  $T$ , (e) reference yield surface size  $p_c$  against  $T$ , and (f) sensitivity state variable  $s_{ep}$  against  $T$  for  $R = 0$  and  $R = 1$  cases.

where  $c_v$  is the vertical coefficient of consolidation ( $\text{m}^2/\text{s}$ ) and  $t$  is the dissipation time (s). The initial  $c_v$  value was calculated from the parameters as:

$$c_v = \frac{k_s p'_0}{\lambda \gamma_w} \quad (21)$$

in which  $k_s$  is permeability of the soil taken as  $1 \times 10^{-9}$  m/s,  $p'_0$  is initial mean effective stress, and  $\gamma_w$  is the unit weight of water.

The re-consolidation path in  $\ln(1+e)$  -  $p'$  space for the analysis with  $R = 1$  follows the unload-reload line before moving parallel to the initial  $K_0$  normal compression line (see Fig. 14c), demonstrating a significant increase in the yield surface size  $p_{cs}$  ( $= s_{ep} \times p_c$ ) due to recovery of the sensitivity state variable  $s_{ep}$  (see Fig. 14d, f). The recovery of the sensitivity overrides the plastic volumetric hardening and also leads to smaller creep volumetric plastic strains, and therefore a negligible change in  $p_c$  is observed until the stress path reaches the  $K_0$  NCL at which plastic strains begin to occur (see Fig. 14e). On the

other hand, the  $R = 0$  analysis demonstrates a stress path typical of the basic SMCC model, which is bound by an NCL defined by the current sensitivity (i.e.  $\approx 1.5$  at invert level at the beginning of consolidation), with higher plastic volumetric hardening (thus higher increase in  $p_c$ ) and higher decrease in  $e$ , and almost no change in  $s_{ep}$ . The dissipation path in  $\ln(1+e)$  -  $p'$  space starts with a path gradient similar to the URL, further follows a stress path with slope higher than the URL before finally becoming parallel to the initial  $K_0$  normal compression line when significant plastic strains develop (see Fig. 14c).

These results can be further illustrated by the contours of  $s_u/s_{ui}$  following the undrained remoulding and re-consolidation stages. Fig. 15a shows the degradation of shear strength due to remoulding, with a fully remoulded state (i.e.  $s_u/s_{ui} = 1/S_{T-bar} = 0.4$ ) at the mid-depth of the T-bar cycling path and no change in strength at far field locations. The recovered post-consolidation strength  $s_u/s_{ui}$  obtained in the analysis with  $R = 0$  is less than  $s_{ui}$  in the entirety of the remoulded area and near full strength regain occurs at the invert level (see Fig. 15b). In contrast

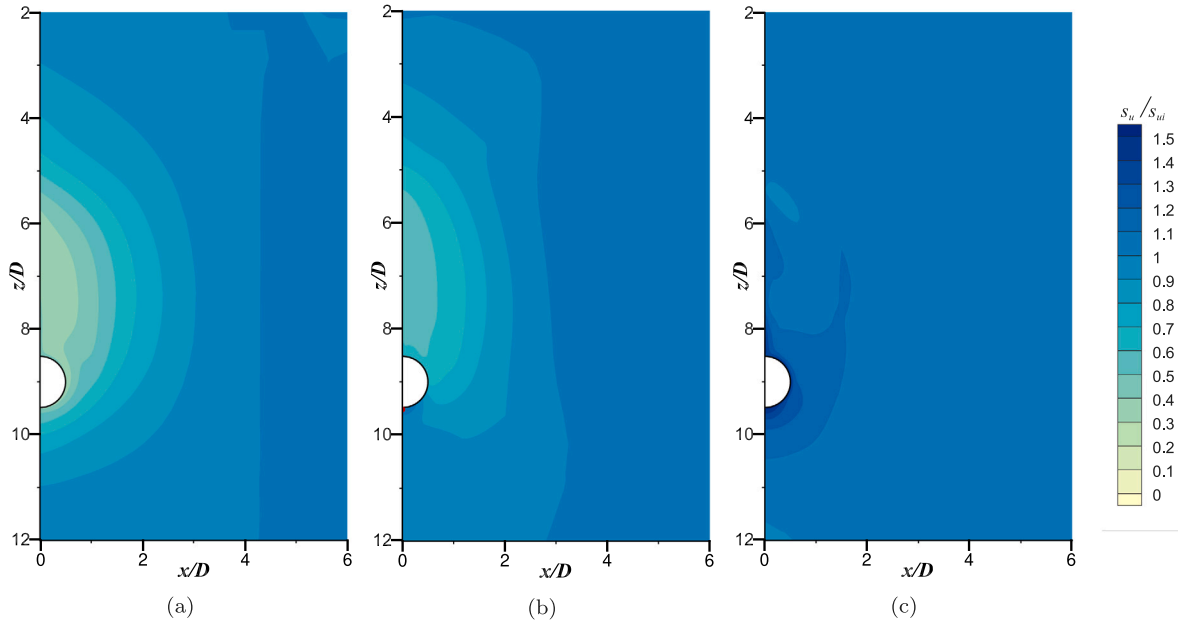


Fig. 15. Distribution of the current undrained shear strength ( $s_u$ ) normalised by the intact undrained shear strength ( $s_{ui}$ ) in NC kaolin clay after: (a) remoulding; (b) re-consolidation with  $R = 0$ ; and (c) re-consolidation with  $R = 1$ .

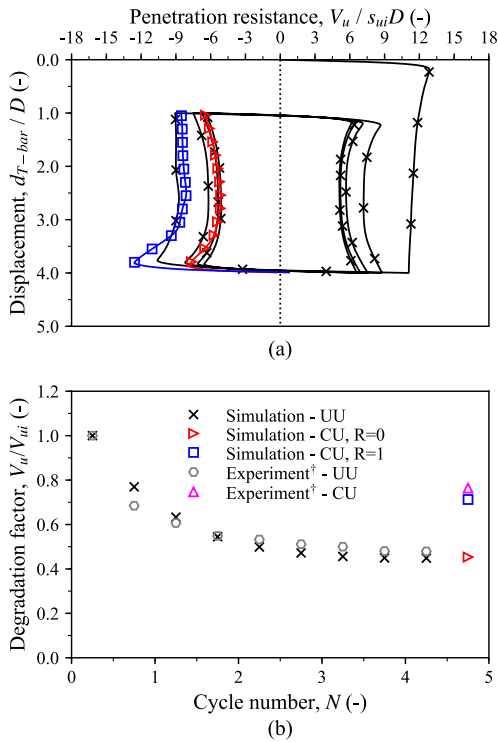


Fig. 16. Cyclic undrained and consolidated-undrained T-bar penetration in OC kaolin clay with  $OCR = 1.5$ : (a) penetration resistance, and (b) strength degradation factor.

a higher regain in  $s_u/s_{ui}$  occurs for the analysis with  $R = 1$ , with  $s_u$  slightly higher than  $s_{ui}$  in the remoulded soil (see Fig. 15c). Values of  $s_u/s_{ui}$  as high as 1.5 are obtained in the soil where the T-bar was parked during consolidation. This is in line with the strength recovery observed in the experiment. Therefore, the model variant allowing some recovery of the sensitivity predicts the strength degradation due to remoulding and the re-consolidation induced regain of strength very

closely compared to the response obtained experimentally from the penetrometer test.

#### 4.4.2. Lightly over-consolidated conditions

A T-bar penetrometer test performed in lightly over-consolidated UWA kaolin clay (Hodder et al., 2013) was simulated with the same model parameters as the NC case as provided in Table 2. The viscoplastic model is mainly applicable to NC soft soils; it does not predict the viscoplastic strains inside the yield surface and therefore is not able to capture the creep and stress relaxation aspects of OC clays. However, the application of this model to predict the influence of ultra high strain rates (4–5 log cycles higher than the reference laboratory strain rate of about 1–3%/h), which is the main feature of these simulations in this paper, can still be justified as negligible viscoplastic strains occur inside the yield surface even for NC soils. The main objective of this simulation was to investigate the validity of the sensitivity recovery rule in OC soil conditions. The numerical modelling details are identical to the simulation of NC kaolin described earlier, except that an OCR of 1.5 was adopted, which is representative of the OCR present at the depth of the cycles in the T-bar experiment.

The results of the simulation ( $V_u/s_{ui}D$  vs.  $d_{T-bar}/D$  and  $V_u/V_{ui}$  vs.  $N$ ) are presented in Fig. 16 for the analyses with  $R = 0$  and  $R = 1$ . The resistance degradation factor  $V_u/V_{ui}$  matches the experiment fairly well. This match was obtained from a simulation using the softening parameters identified from a T-bar test performed in the same clay but under a completely different stress state performed almost 10 years later. This again suggests (as noted by Einav and Randolph, 2005) that the T-bar test is the best candidate for identifying the constitutive model parameters related to strength degradation. Re-consolidation analyses were performed following the undrained cycles, leading to changes in the effective stresses and other soil state variables and thus shear strength, which are further illustrated by the stress paths in Fig. 17 and contours of  $s_u/s_{ui}$  in Fig. 18. The consolidated-undrained T-bar resistance for the  $R = 0$  case increase negligibly (see the  $V_u/V_{ui}$  value represented by red triangle marker in Fig. 16b). For the analysis with  $R = 1$ , however, the  $V_u/s_{ui}D$  value at the middle of the cyclic zone was a factor of 1.68 times higher than the corresponding value at the remoulded state, which is close to the 1.71 factor observed in the experiment. The dilative nature of the OC clay moderates the



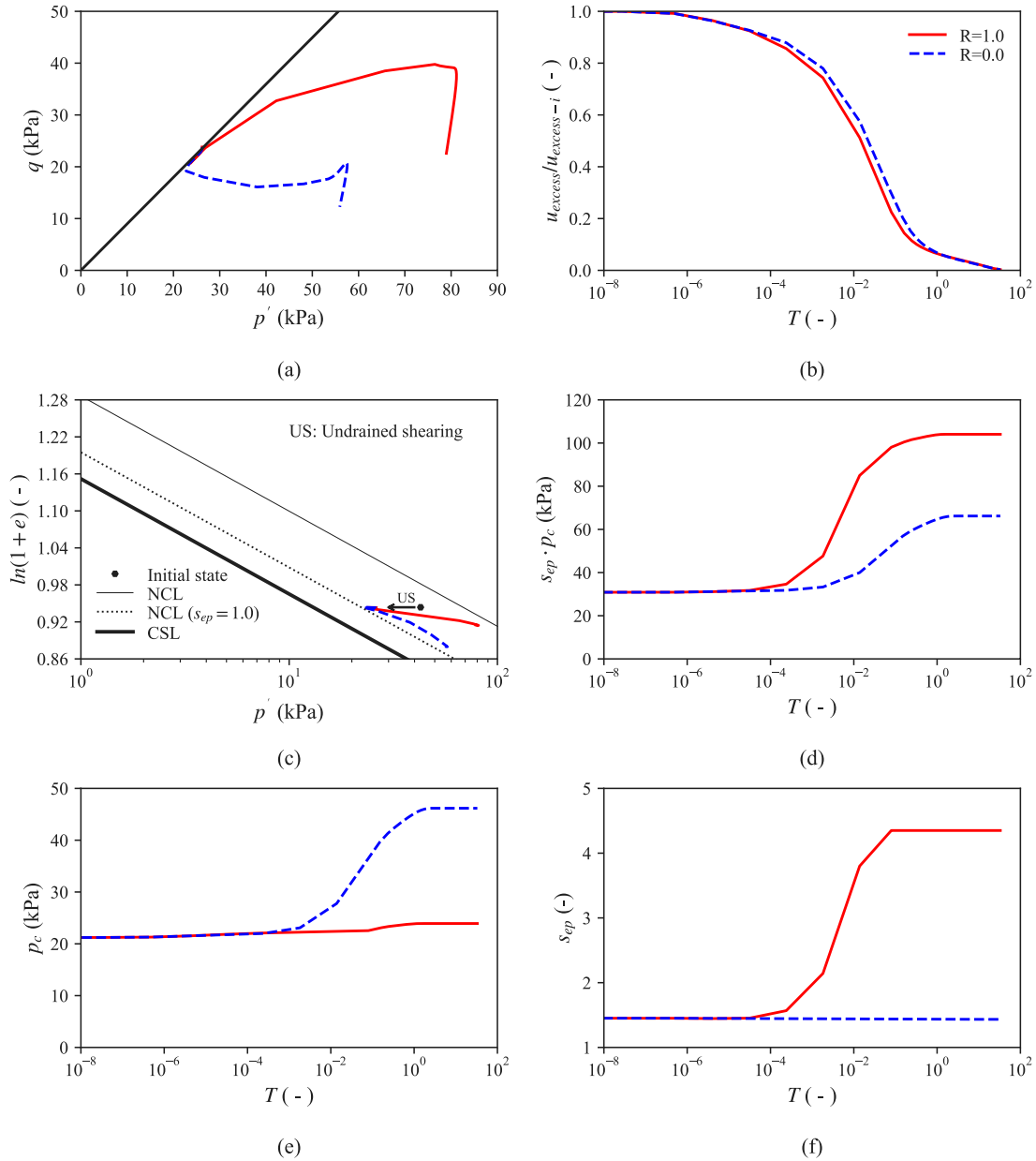


Fig. 17. Re-consolidation response of OC kaolin element beneath T-bar invert: (a) stress path in  $p'$ - $q$  space, (b) normalised excess pore pressure  $u_{\text{excess}}/u_{\text{excess}-i}$  against dimensionless time  $T$ , (c) stress path in  $\ln(1+e)$ - $p'$  space, (d) static yield surface size  $p_{cs}$  against  $T$ , (e) reference yield surface size  $p_c$  against  $T$ , and (f) sensitivity state variable  $s_{ep}$  against  $T$  for  $R=0$  and  $R=1$  cases.

generation of positive excess pore pressures during the undrained cycles, which on dissipation leads to significantly lesser increase in  $p'$ , especially at the mid-depth of the remoulded zone. A modest increase in  $s_u$  due to consolidation in the fully remoulded soil ( $z/D$  between 7–8) can be seen from a comparison of Fig. 18a with b for the simulation with no sensitivity recovery. In contrast, the simulation with sensitivity recovery generates soil strengths that are significantly higher than the remoulded strength (compare Fig. 18a with c). The VRS model with sensitivity recovery during re-consolidation captures the changes in penetration resistance observed in the penetrometer tests performed in both NC and lightly OC kaolin well with consistent parameters.

#### 4.5. T-bar cycling in carbonate silt

A T-bar test performed in the carbonate silt showing partial recovery of sensitivity was also simulated, with model parameters as defined in Table 2. The recovery ratio,  $R$ , was taken as 0.4 and 0.5, which

corresponds to an  $s_u/s_{u-d}$  value of 0.47 and 0.56 according to Eq. (19). These values represent the upper and lower bounds of the range observed in the experiment presented in Fig. 2d.

Fig. 19a presents the penetration resistance factors  $V_u/s_{ui}D$  against  $d_{T-bar}/D$  for the UU and CU numerical analyses with  $R=0$ ,  $R=0.4$ , and  $R=0.5$  conditions. The obtained resistance variation factors  $V_u/V_{ui}$  compared against the experiment are shown in Fig. 19b. The undrained resistance factor,  $V_u/s_{ui}D$ , achieves a peak value of  $\approx 16$  which is higher than a value of about 13 obtained for the NC kaolin due to higher strain rate dependency for the silt, before degrading to a value of 3.5 at a fully remoulded state. The UU resistance degradation matches the data extracted from the experiment fairly well. The consolidated-undrained T-bar resistance factor ( $V_u/V_{ui}$ ) obtained for the  $R=0.4$  and  $R=0.5$  cases are 0.65 and 0.70, respectively, which compare favourably with the value of 0.63 obtained from interpretation of the experiment, whereas the resistance factor for the case the case with no

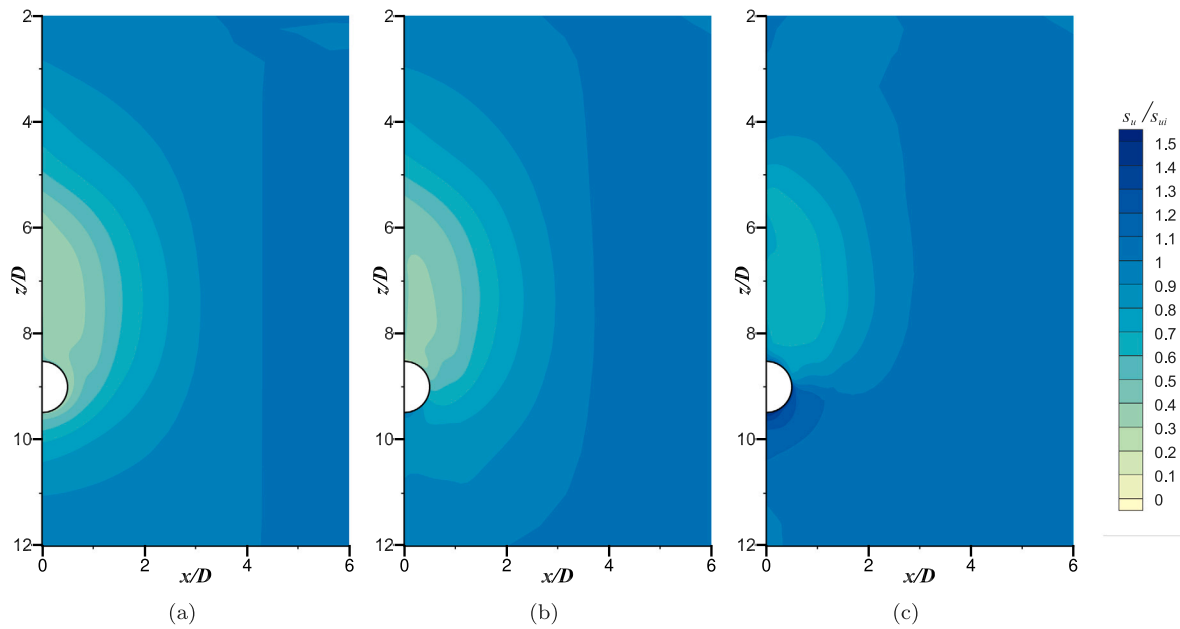


**Fig. 18.** Distribution of the current undrained shear strength ( $s_u$ ) normalised by the initial undrained shear strength ( $s_{ui}$ ) in OC kaolin clay after: (a) remoulding; (b) re-consolidation with  $R = 0$ ; and (c) re-consolidation with  $R = 1$ .

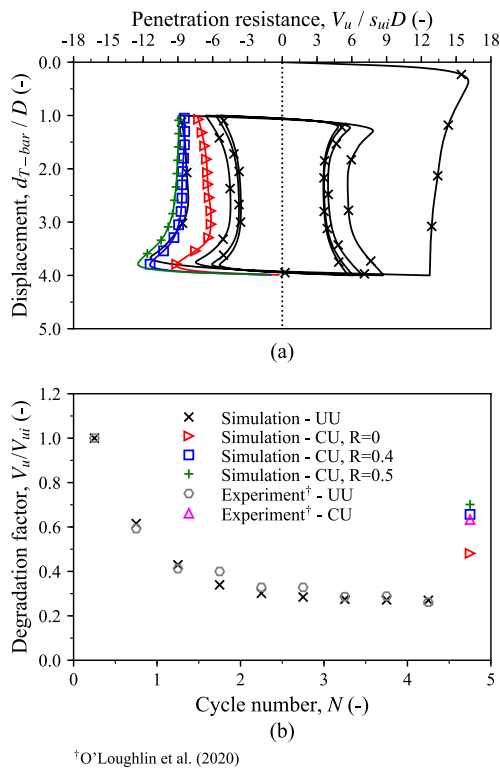


**Fig. 19.** Cyclic undrained and consolidated-undrained T-bar penetration in NC carbonate silt: (a) penetration resistance, and (b) strength degradation/enhancement.

sensitivity recovery is 0.48, which is an underestimation of about 26% compared to the experimentally derived value.

The changes in the shear strength due to dissipation of the excess pore pressures in the consolidation analyses with  $R = 0$  and  $R = 0.4$  are further illustrated using stress and state paths in the soil at T-bar invert level and contours of the current undrained strength  $s_u$  normalised by intact undrained strength  $s_{ui}$  after remoulding and re-consolidation

in Figs. 20 and 21, respectively. From comparison of Fig. 21a, b and c, it can be observed that  $s_u$  first degraded due to remoulding (reaching  $s_u / s_{ui}$  value of 0.2) increases due to re-consolidation, with the maximum regain in  $s_u$  occurring at the T-bar invert level and a slightly higher increase for the analysis with  $R = 0.4$  in comparison to the  $R = 0$  case. The CU T-bar resistance in the silt predicted using the model with  $R = 0$  is comparatively closer to the measured value compared to the equivalent test performed in kaolin clay due to the partial recovery of the sensitivity in case of the silt.

## 5. Conclusions

This paper has presented a viscoplastic strain-softening–hardening constitutive model with non-local softening and consolidation induced recovery of sensitivity in reconstituted sensitive fine-grained soils. It has been assumed that generation of excess pore pressures causes sensitivity and dissipation of the same leads to at least partial recovery of the initial sensitivity. Recovery of this re-consolidation induced sensitivity has been linked, for simplicity, to the dissipation of the excess pore pressures generated during deformation by using the volumetric strains as an indirect measure of the degree of re-consolidation. The model is implemented in the commercial FE code Abaqus via its user specified material subroutine UMAT and the model validation was performed by modelling a CRS oedometer test on St. Herblain clay and triaxial tests on Haney clay. The results demonstrated the model capabilities to predict strain rate effects in standard geotechnical element tests.

To estimate changes in T-bar penetration resistance due to undrained remoulding and re-consolidation of soft clay and silt, the model was applied to simulate three cyclic T-bar penetrometer tests in normally consolidated kaolin clay and carbonate silt and lightly over-consolidated kaolin clay in large deformation finite element analyses using the Re-meshing and Interpolation Technique with Small Strains, and a non-local strain-softening method was adopted in order to obtain FE mesh independent solutions. Monotonic and variable rate T-bar penetration analyses are performed before simulating the cyclic tests to demonstrate the robustness of the numerical implementation of the model and its capability to model strain rate effects.

A number of features and capabilities of the VRS model have been highlighted through these analyses:

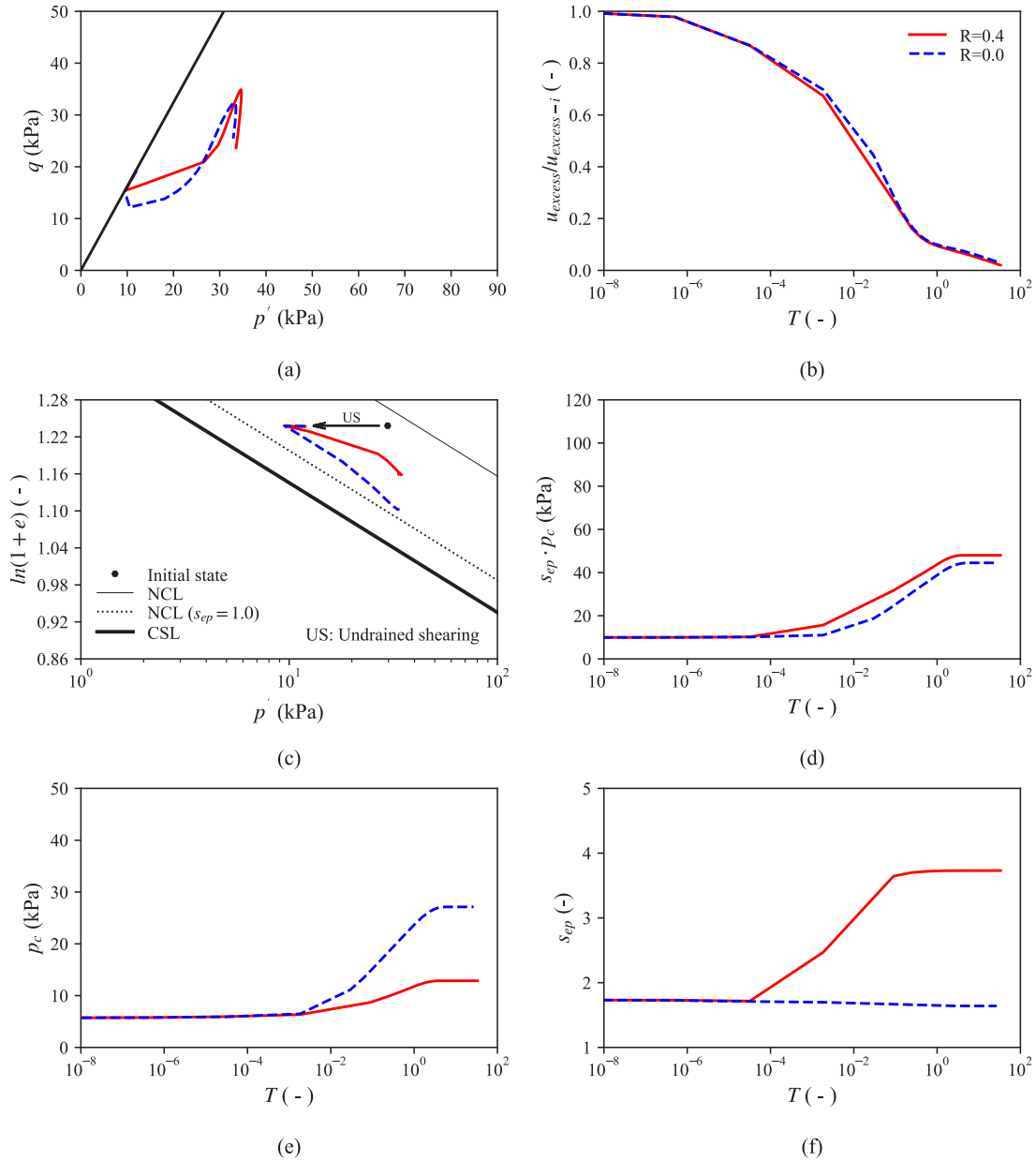


**Fig. 20.** Re-consolidation response of NC carbonate silt element beneath T-bar invert: (a) stress path in  $p' - q$  space, (b) normalised excess pore pressure  $u_{excess}/u_{excess-i}$  against dimensionless time  $T$ , (c) stress path in  $\ln(1+e) - p'$  space, (d) static yield surface size  $p_{cs}$  against  $T$ , (e) reference yield surface size  $p_c$  against  $T$ , and (f) sensitivity state variable  $s_{ep}$  against  $T$  for  $R = 0$  and  $R = 0.4$  cases.

1. The episodic T-bar tests reveal that re-consolidation can lead to full regain of the sensitivity for kaolin clay; however only about 50% of the sensitivity of reconstituted sample can recover in the case of carbonate silt due to the transient (non-recoverable) nature of its inter-particle structure or fabric.
2. Application of the VRS model in T-bar twitch test simulations highlighted the capabilities of the model in estimating strain rate effects.
3. The VRS model with re-consolidation induced regain of the soil sensitivity predicts the consolidated-undrained T-bar resistance very closely compared to experiments in both kaolin clay and a carbonate silt.
4. The model parameter controlling potential recovery of the soil sensitivity  $R$  has been shown to be able to be calibrated from an episodic T-bar penetration test.
5. The VRS model with no allowance for any recovery of the sensitivity (i.e. conventional style model) significantly under-predicts

the consolidated-undrained T-bar resistance in comparison with experimental observations in kaolin clay and carbonate silt.

6. This study sheds light on aspects of large deformation behaviour of soft clay and silt that ought to be considered in the development of new constitutive models for the modelling of geotechnical engineering problems. Specifically this includes the idea that at least some of the strength sensitivity observed in fine-grained soils is likely to be governed by excess pore pressure generation and dissipation.

This research has revealed that ignoring the potential for sensitivity recovery due to consolidation in constitutive modelling could lead to the adoption of conservative strength data in design practice, resulting in the beneficial effects of consolidation induced soil strength regain in 'whole-life' design of offshore infrastructure subjected to large deformations being erroneously ignored.

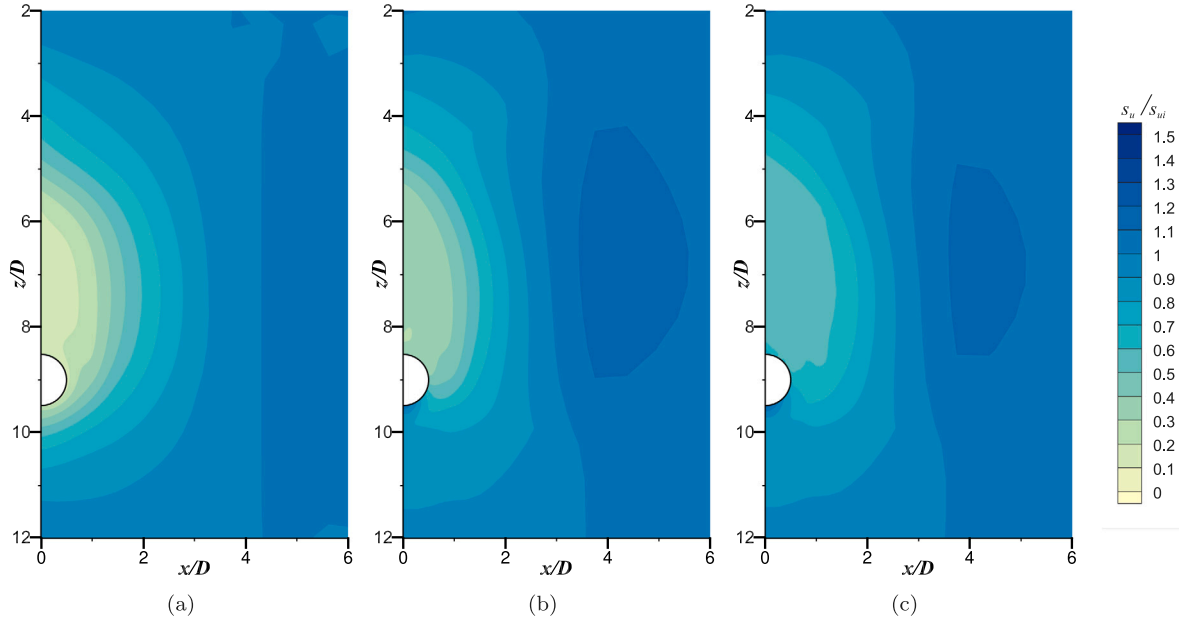


Fig. 21. Distribution of the current undrained shear strength ( $s_u$ ) normalised by the initial undrained shear strength ( $s_{ui}$ ) in NC carbonate silt after: (a) remoulding; (b) re-consolidation with  $R = 0$ ; and (c) re-consolidation with  $R = 0.4$ .

## 6. List of symbols

$a, b, c$  — Fitting parameters for in-situ effective unit weight of soil  
 $A$  — Parameter controlling relative contribution of plastic volumetric and plastic shear strains in softening  
 $c_v$  — Vertical coefficient of consolidation  
 $D_e$  — Constitutive matrix  
 $D$  — T-bar diameter  
 $d_{T-bar}$  — T-bar displacement  
 $e$  — void ratio  
 $\dot{e}$  — Rate of void ratio evolution  
 $f$  — Shape of yield surface  
 $f_d$  — Shape of dynamic loading surface  
 $G$  — Shear modulus  
 $k$  — Sensitivity degradation rate  
 $k_s$  — Soil permeability  
 $K_0$  — Coefficient of lateral pressure at rest  
 $l_c$  — Characteristic length  
 $M$  — Gradient of critical state line  
 $N$  — T-bar penetration cycle number  
 $N_c$  — Breakout factor as suggested by [Randolph and Houlsby \(1984\)](#)  
 $N_{con}$  — Consolidation cycle number  
 $N_v$  — Viscosity exponent  
 $N^*$  — Intercept of the Normal compression line at  $p' = 1$  kPa  
 $p'$  — Mean effective stress  
 $p'_o$  — Initial mean effective stress  
 $p_c$  — Size of reference/static yield surface for  $s_{epi} = 1$   
 $p_{cd}$  — Size of dynamic loading surface passing through the current stress state  
 $p_{cs}$  — Size of reference/static yield surface for  $s_{ep} > 1$ , equal to  $s_{ep} \cdot p_c$   
 $p_r$  — Reference pressure  
 $q$  — Deviatoric stress  
 $q_{pen}$  — T-bar resistance  
 $q_{ref}$  —  $q$  at reference strain rate  
 $r$  — Fitting parameter for in-situ effective unit weight of soil  
 $R$  — Sensitivity recovery parameter  
 $s_{ep}$  — Current value of sensitivity state variable  
 $\dot{s}_{ep}$  — Rate of  $s_{ep}$  evolution  
 $\dot{s}_{epr}$  — Rate of  $s_{ep}$  recovery  
 $s_{epi}$  — Initial value of  $s_{ep}$

$s_{epf}$  — Final value of  $s_{ep}$   
 $S_f$  — Final soil sensitivity on complete remoulding (typically taken as 1)  
 $S_l$  — True soil sensitivity  
 $S_{T-bar}$  — T-bar test derived soil sensitivity  
 $s_u$  — Undrained soil shear strength  
 $s_{ui}$  — Intact  $s_u$   
 $s_{u-d}$  — Theoretical drained limit of  $s_u$   
 $t$  — Pore pressure dissipation time  
 $T$  — Dimensionless pore pressure dissipation time,  $c_v t / D^2$   
 $u_{excess}$  — Excess pore pressure  
 $u_{excess-i}$  — Initial value of  $u_{excess}$   
 $v$  — Penetration rate  
 $V_u$  — Undrained penetration force  
 $V_{ui}$  —  $V_u$  in first T-bar pass  
 $V_{u-ref}$  —  $V_u$  at reference strain rate  
 $z$  — Depth  
 $z_r$  — Depth of the 'rat hole'  
 $\gamma_w$  — Unit weight of water  
 $\gamma'$  — Effective unit weight of soil  
 $\dot{\epsilon}$  — Strain rate  
 $\epsilon_a$  — Axial strain  
 $\dot{\epsilon}^e$  — Elastic strain rate  
 $\dot{\epsilon}^{vp}$  — Viscoplastic strain rate  
 $\dot{\epsilon}_q^{vp}$  — Viscoplastic deviatoric strain rate  
 $\dot{\epsilon}_{vs}$  — Equivalent viscoplastic strain rate  
 $\dot{\epsilon}_v$  — Volumetric strain rate  
 $\dot{\epsilon}_v^{vp}$  — Viscoplastic volumetric strain rate  
 $\kappa^*$  — Slope of the unload-reload line in  $\ln(1+e) - \ln p'$  space  
 $\lambda$  — Slope of the Normal compression line in  $e - \ln p'$  space  
 $\lambda^*$  — Slope of the Normal compression line in  $\ln(1+e) - \ln p'$  space  
 $\mu_v$  — Fluidity parameter  
 $\nu$  — Poisson's ratio  
 $\sigma$  — Stress field  
 $\sigma'_v$  — Vertical effective stress  
 $\sigma'_{vo}$  — Initial  $\sigma'_v$   
 $\dot{\sigma}$  — Stress rate  
 $\phi_c$  — Critical state effective friction angle of soil  
 $\phi(F)$  — Overstress function



## CRediT authorship contribution statement

**Vikram Singh:** Methodology, Software, Formal analyses, Visualisation, Writing – original draft, Revisions based on feedback from coauthors. **Sam Stanier:** Conceptualisation, Supervision, Writing – review & editing. **Britta Bienen:** Supervision, Writing – review & editing. **Mark F. Randolph:** Supervision, Writing – review & editing.

## Declaration of competing interest

The authors declare that they have no known competing financial interests or personal relationships that could have appeared to influence the work reported in this paper.

## Acknowledgements

The first author is supported by UWA Scholarship for International Research Fees, University Postgraduate Award and ad hoc top up scholarship. Prior to moving to the University of Cambridge, the second author was supported at the University of Western Australia by an ARC DECRA Fellowship (DE170100119).

## References

- Bažant, Z.P., Jirásek, M., 2002. Nonlocal integral formulations of plasticity and damage: survey of progress. *J. Eng. Mech.* 128 (11), 1119–1149.
- Bjerre, J., Rnningen, J.A., Grimstad, G., Nordal, S., 2018. Effective stress based model for natural soft clays incorporating restructuration. In: *Numerical Methods in Geotechnical Engineering IX*. CRC Press, pp. 179–186. <http://dx.doi.org/10.1201/9781351003629-23>.
- Butterfield, R., 1979. A natural compression law for soils (an advance on e-log p). *Géotechnique* 29 (4), 469–480.
- Chow, S.H., O'Loughlin, C.D., Zhou, Z., White, D.J., Randolph, M.F., 2019. Penetrometer testing in a calcareous silt to explore changes in soil strength. *Géotechnique* 1–14.
- Chung, S.F., Randolph, M.F., Schneider, J.A., 2006. Effect of penetration rate on penetrometer resistance in clay. *J. Geotech. Geoenviron. Eng.* 132 (9), 1188–1196.
- Cocjin, M.L., Gourvenec, S.M., White, D.J., Randolph, M.F., 2014. Tolerably mobile subsea foundations – observations of performance. *Géotechnique* 64 (11), 895–909.
- Cotecchia, F., Chandler, R.J., 2000. A general framework for the mechanical behaviour of clays. *Géotechnique* 50 (4), 431–447. Publisher: ICE Publishing.
- Cudny, M., Vermeer, P.A., 2004. On the modelling of anisotropy and destructuration of soft clays within the multi-laminate framework. *Comput. Geotech.* 31 (1), 1–22.
- Dafalias, Y.F., Manzari, M.T., Papadimitriou, A.G., 2006. SANICLAY: simple anisotropic clay plasticity model. *Int. J. Numer. Anal. Methods Geomech.* 30 (12), 1231–1257.
- Einav, I., Randolph, M.F., 2005. Combining upper bound and strain path methods for evaluating penetration resistance. *Internat. J. Numer. Methods Engrg.* 63 (14), 1991–2016.
- Galavi, V., Schweiger, H.F., 2010. Nonlocal multilaminate model for strain softening analysis. *Int. J. Geomech.* 10 (1), 30–44.
- Garnier, J., Gaudin, C., Springman, S.M., Culligan, P., Goodings, D., König, D., Kutter, B., Phillips, R., Randolph, M.F., Thorel, L., 2007. Catalogue of scaling laws and similitude questions in geotechnical centrifuge modelling. *Int. J. Phys. Model. Geotech.* 7 (3), 01–23.
- Guevara, M., Doherty, J.P., Gaudin, C., Watson, P.G., 2022. Evaluating uncertainty associated with engineering judgement in predicting the lateral response of conductors. *J. Geotech. Geoenviron. Eng.* 148 (5), 05022001.
- Hodder, M.S., White, D.J., Cassidy, M.J., 2013. An effective stress framework for the variation in penetration resistance due to episodes of remoulding and reconsolidation. *Géotechnique* 63 (1), 30–43.
- House, A.R., Oliveira, J.R.M.S., Randolph, M.F., 2001. Evaluating the coefficient of consolidation using penetration tests. *Int. J. Phys. Model. Geotech.* 1 (3), 17–26.
- Hu, Y., Randolph, M.F., 1998. A practical numerical approach for large deformation problems in soil. *Int. J. Numer. Anal. Methods Geomech.* 22 (5), 327–350.
- Jerman, J., Mašin, D., 2020. Hypoplastic and viscoplastic models for soft clays with strength anisotropy. *Int. J. Numer. Anal. Methods Geomech.* 44 (10), 1396–1416.
- Jia, T., 2021. Extended Framework for Predicting the Behaviour of Tolerably Mobile Subsea Foundations (Ph.D. thesis). The University of Western Australia.
- Katona, M.G., 1984. Evaluation of viscoplastic cap model. *J. Geotech. Eng.* 110 (8), 1106–1125.
- Kelln, C., Sharma, J., Hughes, D., 2008. A finite element solution scheme for an elastic-viscoplastic soil model. *Comput. Geotech.* 35 (4), 524–536.
- Mánica, M.A., Gens, A., Vaunat, J., Ruiz, D.F., 2018. Nonlocal plasticity modelling of strain localisation in stiff clays. *Comput. Geotech.* 103, 138–150.
- Mašin, D., 2009. Comparison of predictive capabilities of selected elasto-plastic and hypoplastic models for structured clays. *Soils Found.* 49 (3), 381–390.
- Mašin, D., 2014. Clay hypoplasticity model including stiffness anisotropy. *Géotechnique* 64 (3), 232–238.
- Monforte, L., Ciantia, M.O., Carbonell, J.M., Arroyo, M., Gens, A., 2019. A stable mesh-independent approach for numerical modelling of structured soils at large strains. *Comput. Geotech.* 116, 103215.
- O'Loughlin, C.D., Zhou, Z., Stanier, S.A., White, D.J., 2020. Load-controlled cyclic T-bar tests: a new method to assess effects of cyclic loading and consolidation. *Géotech. Lett.* 10 (1), 7–15.
- Perzyna, P., 1966. Fundamental problems in viscoplasticity. In: Chernyi, G.G., Dryden, H.L., Germain, P., Howarth, L., Olszak, W., Prager, W., Probstein, R.F., Ziegler, H. (Eds.), *Advances in Applied Mechanics*, Vol. 9. pp. 243–377.
- Ragni, R., Wang, D., Mašin, D., Cassidy, M.J., Bienen, B., 2015. Modelling the effects of pauses during spudcan penetration on the further installation behaviour. In: *Proc. 15 th International Conference of Jack-Up Platform*, London, UK, Paper No. 15.
- Randolph, M.F., 2004. Characterisation of soft sediments for offshore applications. In: *Proceedings of the 2nd International Conference on Site Characterization*. Millpress Science, pp. 209–232.
- Randolph, M.F., Houlsby, G.T., 1984. The limiting pressure on a circular pile loaded laterally in cohesive soil. *Géotechnique* 34 (4), 613–623.
- Randolph, M.F., Low, H., Zhou, H., 2007. In situ testing for design of pipeline and anchoring systems. In: *Proceedings of the 6th International Conference on Offshore Site Investigation and Geotechnics*, London. pp. 251–262.
- Rangeard, D., Hicher, P.Y., Moulin, G., 2002. Identification des Caractéristiques Hydro-Mécaniques d'une Argile par Analyse Inverse d'Essais Pressiométriques (Ph.D. thesis). Ecole Centrale de Nantes et l'Université de Nantes.
- Reid, D., 2021. Request for use of old kaolin DSS tests data.
- Rezania, M., Taiebat, M., Poletti, E., 2016. A viscoplastic SANICLAY model for natural soft soils. *Comput. Geotech.* 73, 128–141.
- Roscoe, K.H., Burland, J., 1968. On the generalized stress-strain behavior of wet clays. *Eng. Plast.* 539–609.
- Sabetamal, H., Carter, J.P., Zhang, X., Sheng, D., 2021. Coupled analysis of full flow penetration problems in soft sensitive clays. *Comput. Geotech.* 133, 104054.
- Singh, V., Stanier, S., Bienen, B., Randolph, M.F., 2021. Modelling the behaviour of sensitive clays experiencing large deformations using non-local regularisation techniques. *Comput. Geotech.* 133, 104025.
- Suebsuk, J., Horpibulsuk, S., Liu, M.D., 2010. Modified structured cam clay: A generalised critical state model for destructured, naturally structured and artificially structured clays. *Comput. Geotech.* 37 (7), 956–968.
- Summersgill, F.C., 2014. Numerical Modelling of Stiff Clay Cut Slopes with Nonlocal Strain Regularisation (Ph.D. thesis). Imperial College London.
- Vaid, Y.P., Campanella, R.G., 1977. Time-dependent behavior of undisturbed clay. *J. Geotech. Eng. Div.* 103 (7), 693–709.
- Vermeer, P., Neher, H.P., 1999. A soft soil model that accounts for creep. In: *Proc Plaxis Symposium 'beyond 2000 in Computational Geotechnics'*, Amsterdam. pp. 249–262.
- Wheeler, S.J., Nääänen, A., Karstunen, M., Lojander, M., 2003. An anisotropic elastoplastic model for soft clays. *Can. Geotech. J.* 40, 403–418. Publisher: NRC Research Press Ottawa, Canada.
- White, D.J., Hodder, M., 2010. A simple model for the effect on soil strength of episodes of remoulding and reconsolidation. *Can. Geotech. J.* 47 (7), 821–826. <http://dx.doi.org/10.1139/T09-137>, URL: <https://www.nrcresearchpress.com/doi/10.1139/T09-137>. Publisher: NRC Research Press.
- Yin, Z.Y., Chang, C.S., Karstunen, M., Hicher, P.Y., 2010. An anisotropic elastic-viscoplastic model for soft clays. *Int. J. Solids Struct.* 47 (5), 665–677.
- Yin, Z.Y., Hicher, P.Y., 2008. Identifying parameters controlling soil delayed behaviour from laboratory and in situ pressuremeter testing. *Int. J. Numer. Anal. Methods Geomech.* 32 (12), 1515–1535.
- Yin, Z.Y., Hicher, P.Y., Riou, Y., Huang, H.W., 2006. An elasto-viscoplastic model for soft clay. In: *GeoShanghai International Conference 2006*. Shanghai, China, pp. 312–319.
- Zhou, H., Randolph, M.F., 2009. Numerical investigations into cycling of full-flow penetrometers in soft clay. *Géotechnique* 59 (10), 801–812.
- Zhou, Z., White, D.J., O'Loughlin, C.D., 2019. An effective stress framework for estimating penetration resistance accounting for changes in soil strength from maintained load, remoulding and reconsolidation. *Géotechnique* 69 (1), 57–71.